ORIGINAL ARTICLE

Evgeni Trofimov · Anna Vainchtein

Shocks versus kinks in a discrete model of displacive phase transitions

Abstract We consider dynamics of phase boundaries in a bistable one-dimensional lattice with harmonic long-range interactions. Using Fourier transform and Wiener–Hopf technique, we construct traveling wave solutions that represent both subsonic phase boundaries (kinks) and intersonic ones (shocks). We derive the kinetic relation for kinks that provides a needed closure for the continuum theory. We show that the different structure of the roots of the dispersion relation in the case of shocks introduces an additional free parameter in these solutions, which thus do not require a kinetic relation on the macroscopic level. The case of ferromagnetic second-neighbor interactions is analyzed in detail. We show that the model parameters have a significant effect on the existence, structure, and stability of the traveling waves, as well as their behavior near the sonic limit.

Keywords Kinks · Shocks · Displacive phase transitions · Kinetic relation · Dispersion · Nonlinear waves

1 Introduction

Many materials are capable of undergoing displacive phase transitions which change the symmetry of the crystal lattice through a diffusionless coordinated motion of atoms. The best known example of such transitions is the martensitic transformation in shape memory alloys. A signature feature of these materials is the hysteresis they exhibit in response to cyclic loading due to the energy dissipated by moving phase boundaries [17].

In continuum elasticity theory displacive phase transitions are typically modeled via a nonconvex elastic energy density, where each convex region corresponds to a different material phase, and the phase boundaries are described as moving discontinuities of the deformation gradient. This approach has been quite successful in predicting the complex equilibrium microstructures observed in martensites [3]. However, extending it to dynamics is problematic due to the failure of the classical theory to describe the dissipative phenomena inside a phase transition front. Although the theory shows that the rate of dissipation must be nonzero, it provides no information about either the origin of dissipation or its dependence on the interface dynamics. To illustrate this fundamental problem, it suffices to consider longitudinal deformation of a homogeneous bar with a unit cross-section and initial density $\rho > 0$. Let $u(x, t)$ be the displacement of a reference point x at time t, and introduce the strain field $w(x, t) = u_x(x, t)$ and the velocity field $v(x, t) = u_t(x, t)$, where $u_t \equiv \partial u/\partial t$ and $u_x \equiv \partial u/\partial x$. The total energy of the bar is

Communicated by Prof. Marshall Slemrod.

E. Trofimov · A. Vainchtein (✉)
Department of Mathematics, University of Pittsburgh, Pittsburgh, PA 15260, USA
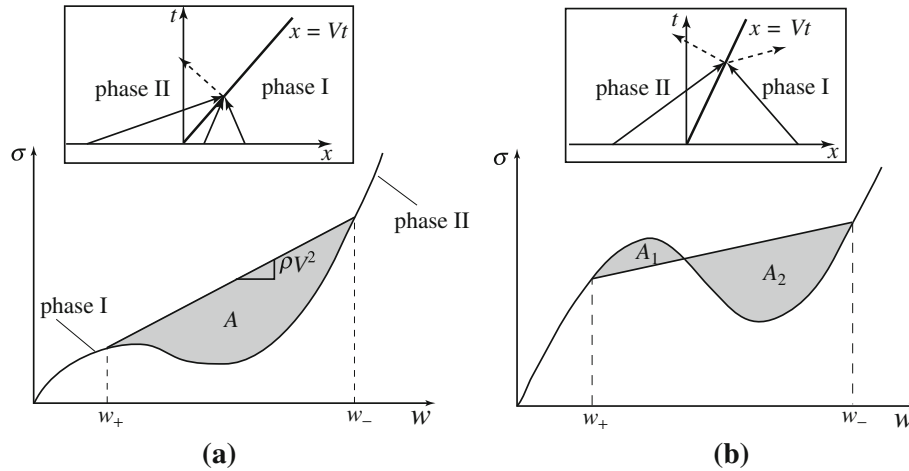E-mail: aav4@pitt.edu

E. Trofimov
E-mail: evt3@pitt.edu

Fig. 1 The macroscopic stress–strain law and the Rayleigh line connecting the strains ahead and behind a phase boundary. **a** An interphase shock. The driving force equals the shaded area A and depends on w_+ and V. **b** A kink, or a subsonic phase boundary. The driving force equals the difference $A_2 - A_1$ between the shaded areas and is determined only by the phase boundary velocity V, which needs to be specified. Insets: schematic representation of incoming and outgoing characteristics in each case

$$\mathcal{E} = \int \left[\frac{\rho v^2}{2} + \phi(w) \right] dx, \tag{1}$$

where $\phi(w)$ is the elastic energy density. To model phase transitions, we follow [6] and assume that $\phi(w)$ is nonconvex, so that the stress–strain relation $\sigma(w) = \phi'(w)$ is non-monotone, as shown in Fig. 1.

The regions where $\sigma'(w) > 0$ correspond to two material phases, phase I and phase II. The balances of mass and linear momentum yield the p-system

$$w_t = v_x, \quad \rho v_t = (\sigma(w))_x. \tag{2}$$

Due to the non-monotonicity of $\sigma(w)$, this is a mixed-type hyperbolic–elliptic system. Initial value problems associated with such equations are known to be ill-posed whenever they lead to the appearance of discontinuities that violate the Lax condition [5,12,16,27].

To see this, consider a strain discontinuity propagating along the bar with a constant velocity $V > 0$. Let $[\![f]\!] \equiv f_+ - f_-$ denote the difference between the limiting values f_+ and f_- of a function $f(x)$ to the right and to the left of the discontinuity and $\{f\} \equiv (f_+ + f_-)/2$ denote their average value. On the discontinuity the balance laws reduce to the Rankine–Hugoniot jump conditions

$$[\![v]\!] + V[\![w]\!] = 0, \quad \rho V[\![v]\!] + [\![\sigma(w)]\!] = 0. \tag{3}$$

In addition, the entropy condition requires that the rate of energy dissipated by the discontinuity is nonnegative:

$$R = GV \geq 0, \tag{4}$$

where

$$G = [\![\phi(w)]\!] - \{\sigma(w)\}[\![w]\!] \tag{5}$$

is the driving (configurational) force.

Two types of discontinuities need to be considered separately. The first one is a classical *shock* whose velocity satisfies the inequality $c_+ < V < c_-$, where c_+ and c_- denote the sound speeds in front and behind the shock: $c_\pm = \sqrt{\sigma'(w_\pm)/\rho}$. If the strains w_+ and w_- are in two different phases, this discontinuity represents an intersonic phase boundary (see Fig. 1a). If they are in the same phase, the shock is a sound wave. In either case, a shock satisfies the Lax condition, and its parameters can be uniquely found from the above conditions. Indeed, the five parameters—the velocities $v_\pm$ and strains $w_\pm$ in front and behind the shock and its speed V—can be found from the two jump conditions (3) on the shock and the conservation laws along the three incoming characteristics (see the inset in Fig. 1a). A *kink*, or a subsonic discontinuity (also known in the literature as an undercompressed shock), is a different type of discontinuity that represents phase boundaries

observed in martensites (see Fig. 1b). The kinks satisfy $V < c_+$ and $V < c_-$, meaning that they violate the Lax condition. One can see that this type of discontinuities are the ones leading to a one-parameter family of solutions of the initial value problem. Indeed, since there are now only two incoming characteristics (Fig. 1b), the classical theory provides only four conditions, while we still have five unknowns [27]. To close the system, one thus needs to supplement the theory with an additional *kinetic relation* specifying the dependence of the driving force on the velocity of the phase boundary [1,26]:

$$G = G(V)$$

Once such relation is specified, it determines the strains $w_\pm$ in front and behind the kink for given V and thus fixes the location of the Rayleigh line in Fig. 1b. Since the continuum theory provides no information about the kinetic relation, and the few available experimental data are scattered [15] and mostly rely on indirect measurements [7,8], it is usually obtained from a regularized theory that introduces an internal structure of the discontinuity, e.g., [18,25,29,31].

In this article, we follow the approach of [29] and regularize the continuum model by replacing it with its natural discrete analog, a chain of point masses, each interacting with several neighbors via elastic springs. To model phase transitions, we assume that the interactions between the nearest neighbors are governed by a nonconvex potential, with two convex regions representing two different material phases. The dynamics of the chain is governed by a nonlinear conservative system of ordinary differential equations that replaces the p-system (2) of the classical theory. In the discrete model an isolated phase boundary is represented by a traveling wave front. As the front propagates through the one-dimensional lattice, the nearest-neighbor (NN) springs switch from the low-strain phase I to the high-strain phase II. To derive the kinetic relation, one needs to find the traveling wave solution describing an isolated phase boundary traveling with a given subsonic velocity and use this solution to compute the corresponding driving force. In the discrete model, a propagating phase boundary emits short-length lattice waves that carry energy away from the front [21,29]. On the macroscopic level, these waves are invisible, and the energy radiation is perceived as dissipation. This radiative damping phenomenon is commonly observed when a defect (whether it is a dislocation, a crack or a phase boundary) propagates through a lattice, e.g., [2,4,9–11,13,20].

An exact solution can be obtained using Fourier transform if one considers a biquadratic NN interaction potential, and all other (long-range) interactions are assumed to be governed by quadratic potentials. This was done in [29] for the special case when the elastic moduli κ_I and κ_{II} in the two phases are equal. When the elastic moduli are different, $\gamma = \kappa_{II}/\kappa_I \neq 1$, the problem becomes technically more difficult and requires the use of Wiener–Hopf factorization technique. In the absence of long-range interactions it was studied in [21–23]. The case $\gamma \leq 1$, which allows for only subsonic phase boundaries, was considered, in [21,23], and nontrivial shock solutions, which occur when $\gamma > 1$, were the focus of [22]. However, some important details about existence, structure, and stability of the traveling wave solutions and the fundamental difference between shock and kink solutions remained unclear.

In this work, we allow the elastic moduli to be different while also incorporating the effect of long-range interactions. We obtain the traveling wave solutions for both kinks (for any $\gamma \neq 1$) and interphase shocks (for $\gamma > 1$) in a unified framework. The inclusion of long-range interactions changes the structure of the roots of the dispersion relation and affects both the internal structure of a phase boundary and the frequency of the radiated lattice waves. This influences existence and stability of the steady interface motion at a given speed and the rate of energy dissipated by the moving front.

We derive the kinetic relation for kinks and show that the lack of such relation in case of shocks is due to the different structure of the roots of the dispersion relation in the intersonic regime, which in turn results in different asymptotic behavior of the Wiener–Hopf factorization in the Fourier space. Instead of being constant at infinite wave numbers, as was the case for kinks, both sides of the Wiener–Hopf equation now behave as a linear polynomial. This leads to the additional degree of freedom in the shock problem that is also seen on the continuum level: one of the strains $w_\pm$, say, w_+, can be specified independently of the given V. Since changing w_+ at the same V shifts the Rayleigh line in Fig. 1a parallel to itself, this means that the same shock velocity corresponds to a *set* of values of the driving force instead of a single value. The extra degree of freedom in this case corresponds to the third incoming characteristic which brings additional information about the state in front of the shock and can be interpreted as a non-oscillating "feeding wave" with zero wave number [22].

The model that includes second-neighbor interactions of ferromagnetic type is analyzed in detail. Such interactions introduce an interfacial energy contribution into the problem, which penalizes the formation of many phase boundaries and creates an additional structure around the interface [28]. We analyze the effect of the elastic moduli ratio γ and the parameter β, which measures the strength of second-neighbor interactions, on

the existence of traveling waves solutions of the assumed form. While solutions typically exist when velocities are above a certain threshold, sufficiently small γ or large enough $|\beta|$ result in existence of some low-velocity kinks and non-existence of shocks in a certain velocity interval. We also investigate how kinetic relations for kinks and stability of the constructed solutions are influenced by the two parameters. Stability is studied numerically by checking whether the long-time solutions of the Riemann problem approach the traveling wave solutions. Our results suggest that sufficiently fast kinks and all existing shock solutions are stable. Some of the slower kinks may become stable at smaller γ and larger $|\beta|$. At large $|\beta|$ we also observe non-steady phase boundary motion which is not described by the traveling wave ansatz.

The structure of the article is as follows. The discrete model and the governing equations are formulated in Sect. 2. In Sect. 3, we seek solutions in the form of a traveling wave. Factorization and the Wiener–Hopf technique are applied in Sect. 4 to represent the corresponding equation in Fourier space in the Wiener–Hopf form. In Sect. 5, we construct exact solutions for kinks, including equilibrium states with the corresponding trapping region, and derive the kinetic relation. In Sect. 6, interphase shock solutions are constructed. Example with ferromagnetic second-neighbor interactions is studied in Sect. 7, and stability of the traveling waves is investigated numerically in Sect. 8. The proof of the proposition in Sect. 4 is given in the Appendix.

2 The discrete model

We consider the one-dimensional lattice model that consists of a chain of isolated point masses connected by springs (Fig. 2). Each particle in the chain interacts with its q neighbors on each side. If $u_n(t)$ is the displacement of the nth particle, the total energy of the chain can be written as

$$\mathcal{E} = \varepsilon \sum_{n=-\infty}^{\infty} \left[\frac{\rho \dot{u}_n^2}{2} + \sum_{p=1}^{q} p \phi_p \left(\frac{u_{n+p} - u_n}{p\varepsilon} \right) \right], \tag{6}$$

where ε is the reference interparticle distance and $\phi_p(w)$ is the potential of interaction between pth neighbors. The dynamics of the chain with energy (6) is then governed by the following infinite system of ordinary differential equations:

$$\rho \ddot{u}_n = \frac{1}{\varepsilon} \sum_{p=1}^{q} \left[\phi_p' \left(\frac{u_{n+p} - u_n}{p\varepsilon} \right) - \phi_p' \left(\frac{u_n - u_{n-p}}{p\varepsilon} \right) \right]. \tag{7}$$

To model phase transitions, we assume that the NN interactions are governed by a nonconvex potential $\phi_1(w)$. To obtain an analytic solution, we further assume that $\phi_1(w)$ is biquadratic:

$$\phi_1(w) = \begin{cases} \frac{1}{2}\kappa_{\mathrm{I}} w^2, & w \leq w_{\mathrm{c}}, \quad \text{phase I} \\ \frac{1}{2}\kappa_{\mathrm{II}}(w-a)^2 + \frac{1}{2}\kappa_{\mathrm{I}} w_{\mathrm{c}}^2 - \frac{\kappa_{\mathrm{II}}}{2}(w_{\mathrm{c}}-a)^2, & w \geq w_{\mathrm{c}}, \quad \text{phase II}. \end{cases} \tag{8}$$

Here, $\kappa_{\mathrm{I}} > 0$ and $\kappa_{\mathrm{II}} > 0$ are the elastic moduli in phase I and phase II, respectively, a is the transformation strain, and w_{c} is the critical strain separating phase I from phase II. As in [21–23], we allow the elastic moduli of the two phases to be different ($\kappa_{\mathrm{I}} \neq \kappa_{\mathrm{II}}$) (see Fig. 3). This makes it possible to study both subsonic phase boundaries (kinks) and intersonic ones (shocks).

As in [29], we also include long-range interactions, which are assumed to be harmonic:

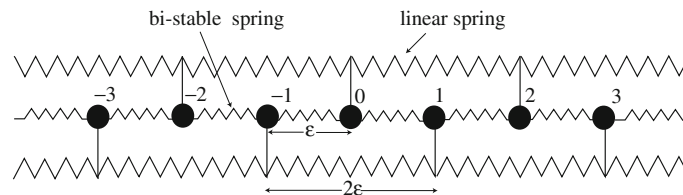$$\phi_p = \frac{1}{2} p \, \mu_p \, w^2, \quad p = 2, \ldots, q, \tag{9}$$

Fig. 2 One-dimensional chain with nearest and next-to-nearest-neighbor interactions ($q = 2$)
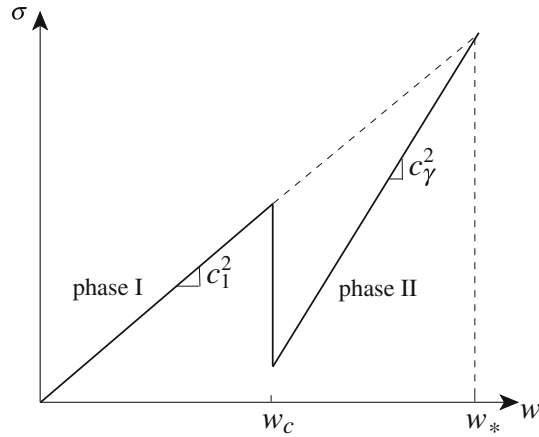
Fig. 3 The bilinear macroscopic stress–strain law

with elastic moduli μ_p chosen so that the uniform deformation $u_n = nw\varepsilon$ of the chain is stable for $w \neq w_c$.

Let

$$w_n = \frac{u_n - u_{n-1}}{\varepsilon}$$

denote the strain in the nth NN spring. We introduce dimensionless variables

$$\tilde{u}_n = \frac{u_n}{\varepsilon a}, \quad \tilde{w}_n = \frac{w_n}{a}, \quad \tilde{t}_n = \frac{t\sqrt{\kappa_{\mathrm{I}}}}{\varepsilon\sqrt{\rho}},$$

and the dimensionless parameters

$$\gamma = \frac{\kappa_{\mathrm{II}}}{\kappa_{\mathrm{I}}}, \quad \Omega_p = \frac{\mu_p}{\kappa_{\mathrm{I}}} \quad \text{for} \quad p = 2, \ldots, q \ (\Omega_1 = 1).$$

The parameter $\gamma > 0$ measures the elastic stiffness of phase II relative to phase I, and the parameters Ω_p, $p = 2, \ldots, q$, measure the relative strength of the long-range interactions. Here, we set $\gamma \neq 1$. The equal moduli case $\gamma = 1$ was considered in [29].

In terms of the dimensionless quantities, with the tildes dropped, the system (7) of governing ordinary differential equations becomes

$$\ddot{w}_n = \sum_{p=1}^{q} \Omega_p \left[w_{n+p} - 2w_n + w_{n-p} \right]$$
$$+ (\gamma - 1) \left[\Theta(w_{n+1} - w_c)w_{n+1} - 2\Theta(w_n - w_c)w_n + \Theta(w_{n-1} - w_c)w_{n-1} \right]$$
$$- \gamma \left[\Theta(w_{n+1} - w_c) - 2\Theta(w_n - w_c) + \Theta(w_{n-1} - w_c) \right], \tag{10}$$

where $\Theta(x)$ is the unit step function. This equation for the discrete model replaces the continuum-level partial differential equation $u_{tt} = (\sigma(u_x))_x$ (the rescaled version of the p-system (2)), where the macroscopic stress–strain law is given by

$$\sigma(w) = \sum_{p=1}^{q} p\phi_p'(w) = \begin{cases} c_1^2 w, & w < w_c \\ c_\gamma^2 w - \gamma, & w > w_c. \end{cases} \tag{11}$$

See Fig. 3. Here,

$$c_\alpha = \left(\alpha + \sum_{p=2}^{q} p^2 \Omega_p \right)^{\frac{1}{2}} \tag{12}$$

is the macroscopic sound speed in the phase I when $\alpha = 1$ and in phase II when $\alpha = \gamma$, with $c_\gamma = \sqrt{c_1^2 + \gamma - 1}$. The two lines in (11) intersect at the strain

$$w_* = \frac{\gamma}{\gamma - 1}. \tag{13}$$

The critical strain w_c satisfies $w_c > w_*$ when $\gamma < 1$ and $w_c < w_*$ when $\gamma > 1$.

3 Traveling wave equation

To model an isolated phase boundary moving with a constant velocity V we consider the traveling wave solutions of (10) in the form $w_n(t) = w(\xi)$, $\xi = n - Vt$, with phase II ($w_n > w_c$) behind the moving front ($\xi < 0$) and phase I ahead of it ($\xi > 0$). Substituting this ansatz into (10), we obtain

$$
\begin{aligned}
V^2 w'' &- \sum_{p=1}^{q} \Omega_p \left[w(\xi + p) - 2w(\xi) + w(\xi - p) \right] \\
&= (\gamma - 1) \left[\Theta(-\xi - 1)w(\xi + 1) - 2\Theta(-\xi)w(\xi) + \Theta(-\xi + 1)w(\xi - 1) \right] \\
&\quad - \gamma \left[\Theta(-\xi - 1) - 2\Theta(-\xi) + \Theta(-\xi + 1) \right],
\end{aligned} \tag{14}
$$

a single advance-delay differential equation.

The configuration at $\xi = \pm\infty$ must correspond to stable homogeneous equilibria (constant strains), which due to the Hamiltonian structure of the problem are possibly superimposed with short-wave oscillations with zero average; the averaging is over the largest period of oscillations but can be also defined as

$$\langle w(\xi) \rangle = \lim_{s \to \infty} \frac{1}{s} \int_{\xi}^{\xi + s} w(\zeta) \mathrm{d}\zeta. \tag{15}$$

In terms of averaged quantities we thus obtain the following boundary conditions

$$\langle w(\xi) \rangle \to w_\pm, \quad \text{as} \quad \xi \to \pm\infty, \tag{16}$$

where $w_+ < w_c < w_-$, $w_+ > w_*$ when $\gamma < 1$ and $w_- < w_*$ when $\gamma > 1$. Note that although the original system (7) is nonlinear, the traveling wave equation (14) is linear due to our assumption of linearity in each phase and the known phase distribution for a traveling wave front. The nonlinearity of the problem thus reduces to the phase switch condition

$$w(0) = w_c. \tag{17}$$

Note also that in writing (14) we assumed that the NN springs in front of the moving interface are in phase I and the springs behind it are in phase II. This implies that admissible solutions must satisfy the inequalities

$$w(\xi) < w_c \quad \text{for} \quad \xi > 0 \ (\text{phase I}), \quad w(\xi) > w_c \quad \text{for} \quad \xi < 0 \ (\text{phase II}). \tag{18}$$

Consequently, the mathematical problem reduces to solving (14) subject to (16), (17), and (18).

In what follows, we will consider two types of solutions: a kink (subsonic, $0 < V < c_{\min} = \min\{c_1, c_\gamma\}$) and an interphase shock, which can occur only when $\gamma > 1$ and has intersonic velocity: $c_1 < V < c_\gamma$.

By linearity of (10), the solution in each phase region (i.e., behind and ahead of the moving front) can be represented as a sum of the average strain at infinity and a superposition of linear waves $w_n = \mathrm{e}^{i(\omega t - kn)}$. The dispersion relation for the waves is

$$\omega^2(k) = \begin{cases} 4\sin^2\dfrac{k}{2} + 4\sum_{p=2}^{q} \Omega_p \sin^2\dfrac{pk}{2}, & \text{phase I}, \\[4mm] 4\gamma \sin^2\dfrac{k}{2} + 4\sum_{p=2}^{q} \Omega_p \sin^2\dfrac{pk}{2}, & \text{phase II}. \end{cases} \tag{19}$$

Note that stability of the uniform deformation in each phase means that $\omega^2(k) > 0$ must hold for all $k \in (0, \pi]$ [30]. In order for the linear modes to be compatible with the traveling waves ansatz, their phase velocity $V_p(k, V) = \omega/k$ must be equal to V. This gives the restriction on the admissible wave numbers in the form $g_1(k, V) = 0$ in phase I ($\xi > 0$) and $g_\gamma(k, V) = 0$ in phase II ($\xi < 0$), where

$$g_\alpha(k, V) = -V^2 k^2 + 4\alpha \sin^2 \frac{k}{2} + 4 \sum_{p=2}^{q} \Omega_p \sin^2 \frac{pk}{2}, \quad \alpha = 1, \gamma. \tag{20}$$

To find the solution we set $w(\xi) = w_+ + h(\xi)$ and apply the generalized Fourier transform to (14). Let $\hat{h}(k, V) = \mathcal{F}[h(\xi)] = \int_{-\infty}^{\infty} h(\xi) e^{ik\xi} d\xi = \hat{h}_-(k, V) + \hat{h}_+(k, V)$, where $\hat{h}_\pm(k, V) = \mathcal{F}[\Theta(\pm\xi)h(\xi)]$. Standard properties of the Fourier transform yield

$$g_1(k, V)\hat{h}_+(k, V) + g_\gamma(k, V)\hat{h}_-(k, V) = (w_+ - w_*) \frac{1}{ik} (g_1(k, V) - g_\gamma(k, V)).$$

where we used (20). Dividing both sides by $g_\gamma(k, V)$ and introducing the function

$$L(k, V) = \frac{g_1(k, V)}{g_\gamma(k, V)}, \tag{21}$$

we obtain the equation

$$L(k, V)\, \hat{h}_+(k, V) + \hat{h}_-(k, V) = (w_+ - w_*) \frac{1}{ik} (L(k, V) - 1). \tag{22}$$

We want to solve this equation for two unknown functions $\hat{h}_+(k, V)$ and $\hat{h}_-(k, V)$. This can be done by applying the Wiener–Hopf technique, as described in the next section.

4 Wiener–Hopf technique and factorization

Consider the equation

$$S_+(k)\, H_+(k) = S_-(k)\, H_-(k), \tag{23}$$

where the functions $H_+(k)$, $H_-(k)$ are unknown and $S_+(k)$ and $S_-(k)$ are given. We assume that the left-hand side is regular (meaning it is analytic and has no zeroes or poles) on $\mathbb{C}^+ \bigcup \mathbb{R}$, and the right-hand side is regular on $\mathbb{C}^- \bigcup \mathbb{R}$. Here, $\mathbb{C}^+, \mathbb{C}^-, \mathbb{R}$ denote the upper half of the complex plane (Im $k > 0$), the lower half (Im $k < 0$) and the real line, respectively. Since both sides are defined and regular on $\mathbb{R}$, there exists a unique analytic continuation function $Q(k)$ defined on the whole complex plane that equals to the right-hand side of (23) in the upper half plane and to the left-hand side of (23) in the lower half plane. If the function $Q(k)$ grows at infinity not faster than k^n, then by Liouville's theorem it must be a polynomial $p_n(k)$ of degree not higher than n. Assuming that the coefficients for this polynomial can be found and equating both sides of (23) to $p_n(k)$, we can find functions $H_+(k)$ and $H_-(k)$. This is the Wiener–Hopf technique in a nutshell. We remark that it is sufficient to have both sides of (23) regular on an interval on the real line.

To apply the Wiener–Hopf technique to solve the Eq. (22), we need to factor $L(k, V)$ defined in (21) into two functions:

$$L(k, V) = L_-(k, V)L_+(k, V). \tag{24}$$

The domains of regularity of $L_-(k, V)$ and $L_+(k, V)$ will be defined later. To find the factorization (24) we need to study the structure of the roots of the function $g_\alpha(k, V)$ at $\alpha = 1$ and $\alpha = \gamma$ and its dependence on the parameter V.

The function $g_\alpha(k, V)$ has a double root at $k = 0$ which can be factored out by setting

$$g_\alpha(k, V) = (c_\alpha^2 - V^2)\, k^2\, f_\alpha(k, V).$$

Here, $f_\alpha(k, V) = 1 + O(k^2)$ in a small neighborhood of zero, and c_α is given by (12). Then

$$L(k, V) = L_0(V) \frac{f_1(k, V)}{f_\gamma(k, V)}, \tag{25}$$

where

$$L_0(V) = L(0, V) = \frac{c_1^2 - V^2}{c_\gamma^2 - V^2}.$$

The set of all roots of $f_\alpha(k, V)$ coincides with all nonzero roots of $g_\alpha(k, V)$ and has a single accumulation point at infinity. We denote this set $\mathcal{M}_\alpha(V)$. Note that

$$f_\alpha(\bar{k}, V) = \overline{f_\alpha(k, V)} \quad \text{and} \quad f_\alpha(-k, V) = f_\alpha(k, V),$$

which implies that if k is a root, then so are $-k$, $\bar{k}$, and $-\bar{k}$. Thus, the complex roots with nonzero real and imaginary parts appear in quadruples, and the roots with zero real or imaginary parts appear in pairs. We can divide $\mathcal{M}_\alpha(V)$ into two major subsets. The first subset contains all real roots $\pm r_{\alpha,i}$. These roots play a major role in the Hamiltonian dynamics of the chain since they correspond to constant-amplitude waves emitted by a moving phase boundary. We denote the set of all positive real roots by

$$\mathcal{N}_\alpha(V) = \{r : \ g_\alpha(r, V) = 0, \quad \text{Im}\, r = 0, \quad r > 0\}$$

and the set of all negative real roots by $-\mathcal{N}_\alpha(V)$. At nonzero V these sets have a finite number of elements. The remaining non-real roots belong to the set

$$\mathcal{C}_\alpha(V) = \{k : \ g_\alpha(k, V) = 0, \ \text{Im}\, k \neq 0\}.$$

This set includes a finite number of purely imaginary roots $\pm i s_{\alpha,i}$ that provide the monotone structure of the core region around the phase boundary and an infinite number of complex roots $k_{\alpha,i} = \pm r_{\alpha,i} \pm i s_{\alpha,i}$, with nonzero real and imaginary parts, that provide oscillatory contributions to the core. We thus have

$$\mathcal{M}_\alpha(V) = \mathcal{C}_\alpha(V) \cup \mathcal{N}_\alpha(V) \cup -\mathcal{N}_\alpha(V).$$

For real r and $V \geq 0$ the equation $g_\alpha(r, V) = 0$ implicitly defines the continuous curve $V = \hat{V}_\alpha(r)$, where

$$\hat{V}_\alpha(r) = \frac{2}{|r|} \sqrt{\alpha \sin^2 \frac{r}{2} + \sum_{p=2}^{q} \Omega_p \sin^2 \frac{pr}{2}}; \tag{26}$$

the real roots are found by solving $\hat{V}_\alpha(r) = V$ for a given V. Observe that $\hat{V}_\alpha(0) = c_\alpha$, $\hat{V}(2\pi n) = 0$ for integer n, so that the number of roots tends to infinity as $V \to 0$. The curve $\hat{V}_\alpha(r)$ has local maxima and minima, as shown in Fig. 4. The corresponding values of V are called the *resonance velocities*. Note that the inclusion of long-range interactions may result in additional extrema (compare Fig. 4a, b) and change the number of roots for a given V. Branches of non-real roots in the set $\mathcal{C}_\alpha(V)$ bifurcate from the extrema at the resonance velocities. There are also isolated non-real root branches that emanate from $V = 0$.

The function $f_\alpha(k, V)$ is entire and satisfies the conditions of the infinite product theorem [14,24], which we apply to find factorization (24):

$$f_\alpha(k, V) = f_\alpha(0) \exp\left[k \frac{f'_\alpha(0)}{f_\alpha(0)}\right] \prod_{k_{\alpha,i} \in \mathcal{M}_\alpha(V)} \left(1 - \frac{k}{k_{\alpha,i}}\right) e^{k/k_{\alpha,i}}.$$

Due to $f_\alpha(0) = 1$, $f'_\alpha(0) = 0$ and the symmetry of the roots about the origin, the product representation can be simplified to

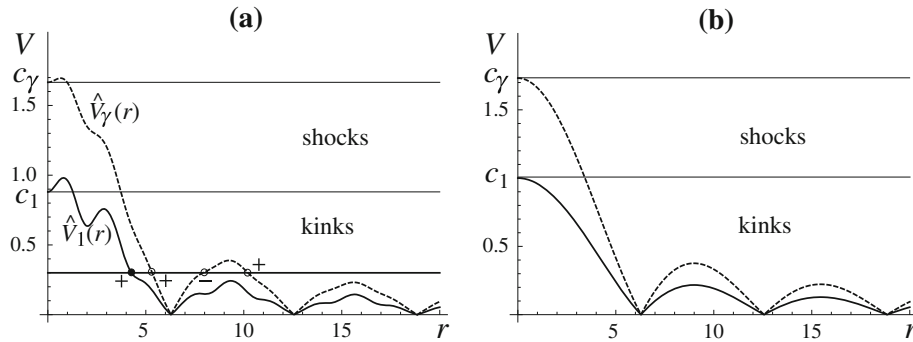$$f_\alpha(k, V) = \prod_{k_{\alpha,i} \in \mathcal{M}_\alpha(V)} \left(1 - \frac{k}{k_{\alpha,i}}\right). \tag{27}$$

Fig. 4 Functions $\hat{V}_1(r)$ (*solid curve*) and $\hat{V}_\gamma(r)$ (*dashed curve*) for positive real roots r, with $\gamma = 3$ and **a** $q = 5$ with $\Omega_2 = -0.3$, $\Omega_3 = 0.3$, $\Omega_4 = -0.1$, and $\Omega_5 = -0.005$; **b** $q = 1$ (no long-range interactions). For given $V > 0$, the roots are found from the intersections with the corresponding horizontal line. For example, at $V = 0.3$ there is one positive real root (*black circle*) of $g_1(r, V)$, located in $\mathcal{N}_1^+(0.3)$, and three positive real roots of $g_\gamma(r, V)$ (*white circles*), distributed to $\mathcal{N}_3^+(0.3)$ and $\mathcal{N}_3^-(0.3)$ according to the signs

We now want to factorize f_α as

$$f_\alpha(k, V) = f_\alpha^+(k, V) \, f_\alpha^-(k, V), \tag{28}$$

so that the function $f_\alpha^\pm(k, V)$ are regular in the union of corresponding halves $\mathbb{C}^\pm$ of the complex plane and a subset of real line that contains an interval. The problem of factorization is thus equivalent to the problem of dividing the roots into two sets and can be done as follows. The set $\mathcal{C}_\alpha(V)$ of all non-real roots can be split into two subsets:

$$\mathcal{C}_\alpha(V) = \mathcal{C}_\alpha^+(V) \cup \mathcal{C}_\alpha^-(V), \quad \text{with} \quad \mathcal{C}_\alpha^\pm(V) = \{k : \ g_\alpha^\pm(k, V) = 0, \ \text{Im} \, k \gtrless 0\}. \tag{29}$$

The positive real roots $\mathcal{N}_\alpha(V)$ have to be distributed according to the radiation condition [19] that places the waves with group velocity

$$V_g = \frac{\partial \omega}{\partial r} = V + \frac{\frac{\partial g_\alpha}{\partial r}(r, V)}{2Vr} \tag{30}$$

larger than the phase velocity V in front, while the waves with $V_g < V$ can appear only behind the phase boundary. Assuming $V > 0$, we obtain that $V_g \gtrless V$ whenever $r \frac{\partial g_\alpha}{\partial r}(r, V) \gtrless 0$. This condition follows from the causality principle [20] and can also be obtained in the limit of zero viscosity [31]. The notation $r \pm i0$ will be used to reflect the effect of the radiation condition on the real roots. The radiation condition yields

$$\mathcal{N}_\alpha(V) = \mathcal{N}_\alpha^+(V) \cup \mathcal{N}_\alpha^-(V),$$

with

$$\mathcal{N}_\alpha^\pm(V) = \left\{ r : \ g_\alpha^\pm(r, V) = 0, \ \text{Im} \, r = 0, \ r > 0, \ \frac{\partial g_\alpha}{\partial r}(r, V) \lessgtr 0 \right\}. \tag{31}$$

This implies that the real roots along the decreasing portions of $\hat{V}_\alpha(r)$ are placed in the set $\mathcal{N}_\alpha^+(V)$, which, as we will see, contributes waves that propagate behind the phase boundary. Meanwhile, the roots along the increasing portions are in $\mathcal{N}_\alpha^-(V)$ and correspond to waves propagating ahead of the moving front. See Fig. 4a for an example. Note that there is a difference in how non-real and real roots are distributed. For any non-real root $k \in \mathcal{C}_\alpha^+(V)$ we have $-k \in \mathcal{C}_\alpha^-(V)$. This is not the case for real roots. If r is a real root that belongs to the set $\mathcal{N}_\alpha^+(V)$, then $-r$ belongs to $-\mathcal{N}_\alpha^+(V)$, not to $\mathcal{N}_\alpha^-(V)$. Denoting by $-\mathcal{N}_\alpha^\pm(V)$ the corresponding sets of negative real roots, we define the subsets

$$\mathcal{M}_\alpha^\pm(V) = \mathcal{C}_\alpha^\pm(V) \cup \mathcal{N}_\alpha^\pm(V) \cup -\mathcal{N}_\alpha^\pm(V), \quad \text{with} \quad \mathcal{M}_\alpha(V) = \mathcal{M}_\alpha^+(V) \cup \mathcal{M}_\alpha^-(V). \tag{32}$$

Factorizing the terms with real and non-real roots separately, we obtain

$$f_\alpha^\pm(k, V) = \prod_{k_{\alpha,i} \in \mathcal{M}_\alpha^\mp(V)} \left(1 - \frac{k}{k_{\alpha,i}}\right) = f_{\alpha,R}^\pm(k, V)\, f_{\alpha,C}^\pm(k, V), \tag{33}$$

where

$$f_{\alpha,R}^\pm(k, V) = \prod_{r_{\alpha,i} \in \mathcal{N}_\alpha^\mp(V)} \left(1 + \frac{(0 \mp ik)^2}{r_{\alpha,i}^2}\right), \quad f_{\alpha,C}^\pm(k, V) = \prod_{k_{\alpha,i} \in \mathcal{C}_\alpha^\mp(V)} \left(1 - \frac{k}{k_{\alpha,i}}\right). \tag{34}$$

Here, we combined the terms with real roots in symmetric pairs using

$$\left(1 - \frac{k}{r \pm i0}\right)\left(1 - \frac{k}{-r \pm i0}\right) = 1 + \frac{(0 \mp ik)^2}{r^2}.$$

The desired factorization (24) is then obtained by substituting (33) and (34) into

$$L_\pm = \sqrt{L_0}\, \frac{f_1^\pm(k, V)}{f_\gamma^\pm(k, V)}. \tag{35}$$

We can now write the Eq. (22) in the Wiener–Hopf form. Dividing both sides of the equation by $L_-(k, V)$ and rearranging the terms, we obtain:

$$L_+(k, V)\left(w_+ - w_* - ik\,\hat{h}_+(k, V)\right) = \frac{1}{L_-(k, V)}\left(w_+ - w_* + ik\,\hat{h}_-(k, V)\right). \tag{36}$$

Note that the functions $L_\pm(k, V)$ are regular in corresponding half planes $\mathbb{C}^\pm$. They are also both regular in the set

$$\mathbb{R}_0 = \mathbb{R} \setminus \bigcup_{r \in \mathcal{N}(V)} (r - \delta/2, r + \delta/2),$$

where $\mathcal{N}(V) = \mathcal{N}_1(V) \cup -\mathcal{N}_1(V) \cup \mathcal{N}_\gamma(V) \cup -\mathcal{N}_\gamma(V)$. This set is the complement on real line to the union of intervals centered at the real roots (which are thus removed), of infinitesimally small length δ each, so the Wiener–Hopf technique is applicable. Thus $L_\pm(k, V)$ are regular in $\mathbb{C}_0^\pm = \mathbb{C}^\pm \cup \mathbb{R}_0$. Since by taking the Fourier transform we have implicitly assumed the same regularity for $\hat{h}_+$ and $\hat{h}_-$, it follows that the left side of (36) is regular in $\mathbb{C}_0^+$, while the right side is regular in $\mathbb{C}_0^-$. Both sides define an analytic function on $\mathbb{R}_0$ and thus can be analytically continued on the whole space $\mathbb{C}$.

To solve the Eq. (36) we need to know the asymptotic behavior of the functions $L_\pm(k, V)$ at infinity and zero. As we will see, these asymptotics are different for shocks and kinks due to the following proposition proved in Appendix.

Proposition *Let $V > 0$ be a non-resonance velocity and let $|\mathcal{N}_\alpha(V)|$ denote the finite number of elements in the set $\mathcal{N}_\alpha(V)$. If V is a kink velocity, $V < \min\{c_1, c_\gamma\}$, we have*

$$|\mathcal{N}_\alpha^+(V)| = |\mathcal{N}_\alpha^-(V)| + 1$$

for both $\alpha = 1$ and $\alpha = \gamma$. If V is a shock velocity, $c_1 < V < c_\gamma (\gamma > 1)$, this equality holds only for $\alpha = \gamma$, while

$$|\mathcal{N}_1^+(V)| = |\mathcal{N}_1^-(V)|.$$

We remark that second equality in the proposition trivially holds for shocks in the case of only NN interactions that was studied in [22]. Indeed, in this case $\hat{V}_1(r)$ always reaches its maximum at $r = 0$, and thus the sets $\mathcal{N}_1^{\pm}(V)$ are both empty for $V > c_1 = \hat{V}_1(0)$. This, however, is not generally true when long-range interactions are included (see Fig. 4a for an example).

To find the asymptotic behavior of $L_{\pm}(k, V)$ at zero and infinity we will follow the procedure given in [19] and use the Cauchy-type integral for factorization. A function $F_\alpha(k, V)$ that satisfies conditions [23]

$$F_\alpha(\pm\infty, V) = 1, \qquad \text{Ind } F_\alpha(k, V) = 0, \tag{37}$$

can be split as $F_\alpha(k, V) = F_\alpha^+(k, V)\, F_\alpha^-(k, V)$, where

$$F_\alpha^{\pm}(k, V) = \exp\left[\pm\frac{1}{2\pi i}\int\limits_{-\infty}^{\infty}\frac{\ln F_\alpha(\xi, V)}{\xi - k \mp i0}\mathrm{d}\xi\right].$$

The function $f_{\alpha, C}(k, V)$ does not satisfy the conditions (37), but the function

$$F_\alpha(k, V) = -\frac{c_\alpha^2 - V^2}{V^2\,(\Pi_\alpha^+)^2\,(\Pi_\alpha^-)^2}(0 - ik)^{2|\mathcal{N}_\alpha^-|}(0 + ik)^{2|\mathcal{N}_\alpha^+|}\, f_{\alpha, C}(k, V), \qquad \Pi_\alpha^{\pm} = \prod_{r_{\alpha,i}\in\mathcal{N}_\alpha^{\pm}} r_{\alpha,i},$$

does and gives the desired factorization for $f_{\alpha, C}(k, V)$:

$$f_{\alpha, C}^{\pm}(k, V) = i\frac{V\,\Pi_\alpha^+\,\Pi_\alpha^-}{\sqrt{c_\alpha^2 - V^2}}(0 - ik)^{-|\mathcal{N}_\alpha^-|}(0 + ik)^{-|\mathcal{N}_\alpha^+|}\, F_\alpha^{\pm}(k, V).$$

We can now find the asymptotes. At infinity we obtain for both kinks and shocks

$$f_{\alpha, C}^{\pm}(k, V) \approx i\frac{V\,\Pi_\alpha^+\,\Pi_\alpha^-}{\sqrt{c_\alpha^2 - V^2}}(0 - ik)^{-|\mathcal{N}_\alpha^-|}(0 + ik)^{-|\mathcal{N}_\alpha^+|},$$

$$f_{\alpha, R}^{\pm}(k, V) \approx \frac{(0 \mp ik)^{2|\mathcal{N}_\alpha^{\mp}|}}{(\Pi_\alpha^{\mp})^2}, \quad k \to \pm i\infty.$$

Due to the above Proposition, this implies different asymptotic behavior for kinks and shocks. For kinks we have

$$f_\alpha^{\pm}(k, V) \approx i\frac{V}{\sqrt{c_\alpha^2 - V^2}}\frac{\Pi_\alpha^{\pm}}{\Pi_\alpha^{\mp}}k^{\mp 1}, \quad k \to \pm i\infty \tag{38}$$

for both $\alpha = 1$ and $\alpha = \gamma$, so that as in [23]

$$L_{\pm}(k, V) \to \mathcal{R}(V)^{\mp 1} \quad \text{as } k \to \pm i\infty, \tag{39}$$

where

$$\mathcal{R}(V) = \frac{\prod\limits_{\mathcal{N}_1^-(V)} r_{1,i}}{\prod\limits_{\mathcal{N}_1^+(V)} r_{1,i}} \cdot \frac{\prod\limits_{\mathcal{N}_\gamma^+(V)} r_{\gamma,i}}{\prod\limits_{\mathcal{N}_\gamma^-(V)} r_{\gamma,i}}. \tag{40}$$

Meanwhile, for shocks Proposition implies that (38) holds only at $\alpha = \gamma$, while

$$f_1^{\pm}(k, V) \to i\frac{V}{\sqrt{c_1^2 - V^2}}\frac{\Pi_1^{\pm}}{\Pi_1^{\mp}}, \quad \text{as } k \to \pm i\infty,$$

so that

$$L_{\pm}(k, V) \approx \mathcal{R}(V)^{\mp 1}k^{\pm 1}, \quad k \to \pm i\infty. \tag{41}$$

At zero the asymptotics are the same for shocks and kinks:

$$L_{\pm}(k, V) \to \sqrt{L_0} \quad \text{as } k \to \pm i0. \tag{42}$$

We can now solve the Eq. (36). Due to the different asymptotics (39) and (41), the solution of (36) is different for kinks and shocks. In what follows, we consider these two cases separately.

5 Kink solutions

5.1 Dynamic solutions

Consider velocities in the kink interval, $0 < V < \min\{c_1, c_\gamma\}$. In this case, the asymptotics (39) at infinity ensure that the analytic continuation of both sides of (36) is likewise bounded at infinity and hence is a constant. The value of this constant A can be found by calculating the values of each side of (36) in the limits $k \to \pm i0$ and $k \to \pm i\infty$. Using (39), (42) and the properties of the Fourier transform [20], we obtain

$$A = \sqrt{L_0(V)}(w_+ - w_*) = \frac{1}{\sqrt{L_0(V)}}(w_- - w_*) = \frac{1}{\mathcal{R}(V)}(w_c - w_*). \tag{43}$$

It follows that

$$w_- = L_0(V)(w_+ - w_*) + w_*, \tag{44}$$

which coincides with the Rankine-Hugoniot condition $V^2 [\![w]\!] = [\![\sigma(w)]\!]$ (obtained by eliminating the particle velocity from the two Rankine-Hugoniot conditions (3) for the rescaled variables) computed for the macroscopic stress–strain relation (11). Equation (43) also implies that the strains $w_\pm$ are determined by the given V:

$$w_+ = \frac{1}{\mathcal{R}(V)\sqrt{L_0(V)}}(w_c - w_*) + w_*, \quad w_- = \frac{\sqrt{L_0(V)}}{\mathcal{R}(V)}(w_c - w_*) + w_*. \tag{45}$$

Equating each side of the Eq. (36) to A from (43), we find the functions $\hat{h}_+(k, V)$ and $\hat{h}_-(k, V)$. Adding them up, we get

$$\hat{h}(k, V) = \hat{h}_+(k, V) + \hat{h}_-(k, V) = \frac{w_+ - w_*}{ik}\sqrt{L_0(V)}\left(L_-(k, V) - \frac{1}{L_+(k, V)}\right). \tag{46}$$

Applying inverse Fourier transform to $\hat{h}(k, V)$, we then obtain

$$w(\xi) = w_+ + \frac{1}{2\pi}\int_\Gamma \hat{h}(k, V)e^{-ik\xi}\,dk, \tag{47}$$

where Γ is the contour that runs in the direction of increasing $\mathrm{Re}\,k$ and coincides with the real line everywhere except near the singular points. To resolve the singularity at $k = 0$, the contour goes below the origin $k = 0$ along a small-radius semicircle in the lower half plane. To resolve the singularities at nonzero real roots according to the radiation condition, the contour passes below all real roots from the sets $\pm\mathcal{N}_1^+(V)$, $\pm\mathcal{N}_\gamma^+(V)$ and above the real roots from the sets $\pm\mathcal{N}_1^-(V)$, $\pm\mathcal{N}_\gamma^-(V)$. This contour deformation effectively shifts the roots to the appropriate sets of singularities, either above ($\mathcal{M}_1^+ \cup \mathcal{M}_\gamma^+$) or below ($\mathcal{M}_1^- \cup \mathcal{M}_\gamma^-$) the contour Γ.

Closing the contour along a semicircle in the upper half plane at $\xi < 0$ and the lower half plane at $\xi < 0$ and using Jordan's lemma and the residue theorem, we obtain the kink solution:

$$(\xi) = \begin{cases} w_- - (w_- - w_*)\displaystyle\sum_{k_{\gamma,i}\in\mathcal{M}_\gamma^+(V)} P_+(k_{\gamma,i}, V)e^{-ik_{\gamma,i}\xi}, & \xi < 0, \\[2ex] w_+ - (w_+ - w_*)\displaystyle\sum_{k_{1,i}\in\mathcal{M}_1^-(V)} P_-(k_{1,i}, V)e^{-ik_{1,i}\xi}, & \xi > 0. \end{cases} \tag{48}$$

Here, we defined

$$P_+(k, V) = \frac{\displaystyle\prod_{k_{1,j}\in\mathcal{M}_1^+(V)}\left(1 - \frac{k}{k_{1,j}}\right)}{\displaystyle\prod_{\substack{k_{\gamma,j}\in\mathcal{M}_\gamma^+(V),\\ j\neq i}}\left(1 - \frac{k}{k_{\gamma,j}}\right)}, \quad P_-(k, V) = \frac{\displaystyle\prod_{k_{\gamma,j}\in\mathcal{M}_\gamma^-(V)}\left(1 - \frac{k}{k_{\gamma,j}}\right)}{\displaystyle\prod_{\substack{k_{1,j}\in\mathcal{M}_1^-(V),\\ j\neq i}}\left(1 - \frac{k}{k_{1,j}}\right)}. \tag{49}$$

Note that in the generic case $q \geq 2$ the continuity of $w(\xi)$ at $\xi = 0$ is ensured by the fact that the sum of all residues is zero:[1]

$$1 - L_0(V) + L_0(V) \sum_{k_{\gamma,i} \in \mathcal{M}_\gamma^+(V)} P_+(k_{\gamma,i}, V) = \sum_{k_{1,i} \in \mathcal{M}_1^-(V)} P_-(k_{1,i}, V).$$

Finally, one needs to check that the formally obtained solution (48) satisfies the admissibility conditions (18) which ensure that the assumed phase distribution holds.

To find the particle velocity $v_n(t) = \dot{u}_n(t)$ we recall that $w_n(t) = u_n(t) - u_{n-1}(t)$, so that $\dot{w}_n = v_n - v_{n-1}$. Using the traveling wave ansatz, we thus obtain the following relation between the particle velocity and the already computed strain profile:

$$v(\xi) - v(\xi - 1) = -V w'(\xi).$$

Solving this equation by Fourier transform and using (46), we obtain

$$v(\xi) = \begin{cases} v_- + \dfrac{V}{2}(w_- - w_*) \displaystyle\sum_{k_{\gamma,i} \in \mathcal{M}_\gamma^+(V)} \dfrac{k_{\gamma,i}}{\sin \frac{k_{\gamma,i}}{2}} P_+(k_{\gamma,i}, V) e^{-ik_{\gamma,i}(\xi+1/2)}, & \xi < -\dfrac{1}{2}, \\[2ex] v_+ + \dfrac{V}{2}(w_+ - w_*) \displaystyle\sum_{k_{1,i} \in \mathcal{M}_1^-(V)} \dfrac{k_{1,i}}{\sin \frac{k_{1,i}}{2}} P_-(k_{1,i}, V) e^{-ik_{1,i}(\xi+1/2)}, & \xi > -\dfrac{1}{2}, \end{cases} \tag{50}$$

where

$$v_+ - v_- = V(w_+ - w_*)(L_0(V) - 1). \tag{51}$$

coincides with the first Rankine-Hugoniot condition for the macroscopic problem, $[\![v]\!] = -V[\![w]\!]$. Recall that the other macroscopic jump condition was recovered by (44). Observe also that by Galilean invariance, v_+ is arbitrary and can be set to zero.

5.2 Kinetic relation

An important feature of the kink solution obtained above is the fact that the strains w_+ and w_- at infinity both depend on the velocity V of the phase boundary via the relations (45). Note that in view of (44) the two relations are not independent. Recall that the traveling wave solution of the discrete problem introduces the structure in the transformation front, replacing the sharp interface representation of a phase boundary in the continuum theory by a transition layer. In particular, the limiting strains $w_\pm$ in the kink solution coincide with the strains ahead of and behind the moving discontinuity in the macroscopic problem and, as we have established, satisfy the same Rankine-Hugoniot jump conditions.

Thus, we can choose either of the relations (45) as a closing *kinetic relation*, which is missing from the continuum theory and relates either w_+ or w_- to V. Once this relation is specified (in this case, derived from the discrete problem), the continuum initial value problem becomes well-posed and has a unique solution.

It is more common to specify the kinetic relation in a different but related form, as a relation between the driving force G on a phase boundary and its velocity V. Using (5) and (11), we obtain the following expression for the driving force:

$$G = \frac{\gamma}{2}(w_+ + w_- - 2w_c) + \frac{\gamma - 1}{2}(w_c^2 - w_+ w_-) \tag{52}$$

Applying (45) we then get the kinetic relation

$$G = G(V) = \frac{\gamma - 1}{2}(w_c - w_*)^2 \left(1 - \frac{1}{\mathcal{R}^2(V)}\right), \tag{53}$$

which reduces to the expression obtained in [29] when $\gamma \to 1$. Note that the driving force is entirely determined by the positive real roots of the dispersion relation, which in turn are determined by V. Recall that these roots

---

[1] In the case of only NN interactions ($q = 1$) we need to add the contribution of the integrals along the semicircles at infinity, which in this case is nonzero at $\xi = \pm 0$ [29].

correspond to the undecaying lattice waves radiated by a moving phase boundary and carrying energy away from it. In fact, the kinetic relation (53) can be derived by accounting for the fluxes of energy carried by the radiative waves, as was done for the case $\gamma = 1$ in [29]. Although discrete system we study is Hamiltonian, and thus conserves energy, on the macrolevel the short-length lattice waves radiated by the phase boundary are not seen, and the energy they carry is thus perceived as lost [20]. This transfer of energy from long to short waves, or the radiative damping phenomenon, as it is known in the physics literature, is responsible for a substantial part of the macroscopic dissipation [10,11].

5.3 Equilibrium states and lattice trapping

As V tends to zero, the kink profile $w_n(t) = w(n - Vt)$ approaches an equilibrium solution w_n satisfying the system of difference equations (10) with the second time derivative in the left-hand side replaced by zero. In the equilibrium states the phase boundary is stationary ($V = 0$), and the jump conditions (3) reduce to $[\![\sigma(w)]\!] = 0$, meaning that

$$c_1^2 w_+ = c_\gamma^2 w_- - \gamma = \sigma, \tag{54}$$

where σ is the stress, which is constant in an equilibrium. The driving force (5) is then given by

$$G = \frac{\sigma^2(1-\gamma)}{2c_1^2 c_\gamma^2} + \frac{\sigma\gamma}{c_\gamma^2} + \frac{\gamma^2}{2c_\gamma^2} + \frac{\gamma-1}{2}w_c^2 - \gamma w_c. \tag{55}$$

Note that at $\gamma \neq 1$ it is a quadratic function of stress. The driving force vanishes at the Maxwell stress

$$\sigma_M = c_1 c_\gamma w_c - \frac{c_1 \gamma}{c_1 + c_\gamma}, \tag{56}$$

which divides the stress–strain curve into two equal areas.

To obtain the equilibrium states with the phase boundary at $n = -1$, we follow [10,29] and replace the continuous Fourier transform by its discrete analog. Using (54), we obtain

$$w_n = \begin{cases} \dfrac{\sigma + \gamma}{c_\gamma^2} - \left(\dfrac{\sigma + \gamma}{c_\gamma^2} - w_*\right) \displaystyle\sum_{k_{\gamma,i} \in F_\gamma^+} \dfrac{k_{\gamma,i}/2}{\sin(k_{\gamma,i}/2)} P_+(k_{\gamma,i}, 0)e^{-ik_{\gamma,i}(n+1/2)}, & n < 0, \\[4mm] \dfrac{\sigma}{c_1^2} - \left(\dfrac{\sigma}{c_1^2} - w_*\right) \displaystyle\sum_{k_{1,i} \in F_1^-} \dfrac{k_{1,i}/2}{\sin(k_{1,i}/2)} P_-(k_{1,i}, 0)e^{-ik_{1,i}(n+1/2)}, & n \geq 0. \end{cases} \tag{57}$$

Here,

$$F_\alpha^\pm = \{k : \ g_\alpha(k, 0) = 0, \ \mathrm{Im}\, k \gtrless 0, \ -\pi \leq \mathrm{Re}\, k \leq \pi\}$$

are the nonzero roots of the dispersion relation (19) in the strip $|\mathrm{Re}\, k| \leq \pi$ (note that there are no nonzero real roots in this region), and $P_\pm(k, 0)$ are given by (49) at $V = 0$. In this case, the real roots in each phase are given by integer multiples of 2π, so that the corresponding terms in (49) cancel out, and the products are thus taken over the sets $\mathcal{C}_\alpha^\pm(0)$.

The admissible values of σ are determined by the requirement that the assumed phase distribution holds:

$$w_n \geq w_c \ \text{ for } \ n \leq -1, \qquad w_n \leq w_c \ \text{ for } \ n \geq 0.$$

If the strain profile is monotone (e.g., when $\Omega_p < 0$ for $p = 2, \ldots q$), these constraints can be replaced by $w_0 \leq w_c$ and $w_{-1} \geq w_c$. In this case, the stress must be within the *trapping region*

$$\sigma_M - \sigma_P^- \leq \sigma \leq \sigma_M + \sigma_P^+ \tag{58}$$

in order for the equilibrium state (57) to exist. Here, σ_P^- and σ_P^+ are the upper and lower Peierls stresses that correspond to $w_0 = w_c$ and $w_{-1} = w_c$, respectively. Under the conditions[2]

$$\sum_{k_{\gamma,i} \in F_\gamma^+} \frac{k_{\gamma,i}/2}{\sin(k_{\gamma,i}/2)} \, P_+(k_{\gamma,i}, 0) e^{ik_{\gamma,i}/2} < 1, \qquad \sum_{k_{1,i} \in F_1^-} \frac{k_{1,i}/2}{\sin(k_{1,i}/2)} \, P_-(k_{1,i}, 0) e^{-ik_{1,i}/2} < 1$$

we obtain

$$\sigma_P^- = c_\gamma (w_c - w_*) \left[c_1 - c_\gamma \left(1 - \sum_{k_{\gamma,i} \in F_\gamma^+} \frac{k_{\gamma,i}/2}{\sin(k_{\gamma,i}/2)} \, P_+(k_{\gamma,i}, 0) e^{ik_{\gamma,i}/2} \right)^{-1} \right],$$

$$\sigma_P^+ = -c_1 (w_c - w_*) \left[c_\gamma - c_1 \left(1 - \sum_{k_{1,i} \in F_1^-} \frac{k_{1,i}/2}{\sin(k_{1,i}/2)} \, P_-(k_{1,i}, 0) e^{-ik_{1,i}/2} \right)^{-1} \right]. \qquad (59)$$

In terms of the driving force, the trapping region (58) corresponds to the interval $G_P^- < G < G_P^+$, where

$$G_P^\pm = \pm \frac{(1-\gamma)\sigma_P^\pm}{c_1 c_\gamma} \left(w_c - w_* \pm \frac{\sigma_P^\pm}{2 c_1 c_\gamma} \right). \qquad (60)$$

One can show that all equilibria in the interior of the region (58) are stable (local minimizers of energy) since all springs are inside their respective wells. A phase boundary may get trapped in one of these stable states until the driving force reaches one of the limiting Peierls values (60). At these values the equilibria become saddle points from which the dynamic solution bifurcates. The phase boundary starts moving to the left ($V < 0$) when $G = G_P^- = G(0-)$ and to the right ($V > 0$) when $G = G_P^+ = G(0+)$.

6 Interphase shocks

Consider now (14) at $\gamma > 1$ and choose a velocity in the shock interval, $c_1 < V < c_\gamma$. In this case, $L_0(V) < 0$ and hence $\sqrt{L_0(V)}$ becomes purely imaginary. Each side of (36) now defines an analytic function which behaves as $O(k)$ at infinity, which implies that this function must be a linear polynomial of k, $p_1(k) = Bk + A$. The constant A is calculated by taking the limit $k \to \pm i0$ of both sides. Since the zero asymptotics (42) are the same for shocks and kinks, the first two equalities in (43) still hold. This means that the constant A is the same, and the Rankine-Hugoniot jump condition (44) again holds. Note, however, that the *third* equality in (43) no longer holds in case of shocks because the asymptotics (41) are now different. Using it, we compute the constant B from

$$B = \lim_{k \to \pm i\infty} \frac{1}{k} \, (L_\pm(k, V))^{\pm 1} \left(w_+ - w_* \mp ik \, \hat{h}_\pm(k, V) \right) = \frac{w_c - w_*}{\mathcal{R}(V)}.$$

Equating both sides of (36) to $Bk + A$, we obtain

$$\hat{h}(k, V) = \hat{h}_+(k, V) + \hat{h}_-(k, V)$$

$$= \frac{w_+ - w_*}{ik} \sqrt{L_0(V)} \left(L_-(k, V) - \frac{1}{L_+(k, V)} \right) + \frac{w_c - w_*}{i\,\mathcal{R}(V)} \left(L_-(k, V) - \frac{1}{L_+(k, V)} \right). \qquad (61)$$

Applying the inverse Fourier transform, Jordan's lemma and the residue theorem as before, we find $w(\xi)$:

$$w(\xi) = \begin{cases} w_- - \displaystyle\sum_{k_{\gamma,i} \in \mathcal{M}_\gamma^+(V)} \left(w_- - w_* + \frac{\sqrt{L_0(V)}}{\mathcal{R}(V)} (w_c - w_*) k_{\gamma,i} \right) P_+(k_{\gamma,i}, V) e^{-ik_{\gamma,i}\xi}, & \xi < 0 \\[4mm] w_+ - \displaystyle\sum_{k_{1,i} \in \mathcal{M}_1^-(V)} \left(w_+ - w_* + \frac{w_c - w_*}{\mathcal{R}(V)\sqrt{L_0(V)}} k_{1,i} \right) P_-(k_{1,i}, V) e^{-ik_{\gamma,i}\xi}, & \xi > 0. \end{cases} \qquad (62)$$

---

[2] We have verified that these inequalities hold in the case $q = 2$ considered in Sect. 7.

Here, $P_\pm(k, V)$ are again given by (49). Observe that in this case

$$\sum_{k_{\gamma,i} \in \mathcal{M}_\gamma^+(V)} P_+(k_{\gamma,i}, V) = 1, \qquad \sum_{k_{1,i} \in \mathcal{M}_1^-(V)} P_-(k_{1,i}, V) = 1. \tag{63}$$

Indeed, consider the integral

$$I_+ = \frac{1}{2\pi i} \int_{\Gamma_+} \frac{L_-(k, V)}{k} \, dk,$$

where we assume that the contour Γ_+ is obtained by closing Γ by a semicircle of infinite radius in the upper half plane. On one hand, the residue theorem yields

$$I_+ = \frac{1}{\mathcal{R}(V)} \left[1 - \sum_{k_{\gamma,i} \in \mathcal{M}_\gamma^+(V)} P_+(k_{\gamma,i}, V) \right].$$

On the other hand, direct evaluation using the fact that for shocks $L_-(k, V) = O(1/k)$ at infinity yields $I_+ = 0$. This gives the first equality in (63). The second one can be shown in the similar way. Note that (63) does not hold for kinks because of the different asymptotics (39). One can also show that

$$\sum_{k_{\gamma,i} \in \mathcal{M}_\gamma^-(V)} k_{\gamma,i} P_-(k_{\gamma,i}, V) = -\mathcal{R}(V)\sqrt{L_0(V)}, \qquad \sum_{k_{\gamma,i} \in \mathcal{M}_\gamma^+(V)} k_{\gamma,i} P_+(k_{\gamma,i}, V) = -\frac{\mathcal{R}(V)}{\sqrt{L_0(V)}}.$$

Along with (63), these conditions ensure that $w(\xi)$ given by (62) is continuous at $\xi = 0$ and that the phase switch condition $w(0) = w_c$ is satisfied.

The particle velocity can be found similarly to the kink case:

$$v(\xi) = \begin{cases} v_- + \dfrac{V}{2} \displaystyle\sum_{k_{\gamma,i} \in \mathcal{M}_\gamma^+(V)} \left(w_- - w_* + \dfrac{\sqrt{L_0(V)}}{\mathcal{R}(V)}(w_c - w_*)k_{\gamma,i} \right) \\ \qquad\qquad\qquad \times \dfrac{k_{\gamma,i} P_+(k_{\gamma,i}, V)}{\sin(k_{\gamma,i}/2)} e^{-ik_{\gamma,i}(\xi+1/2)}, \qquad \xi < -\dfrac{1}{2} \\[2em] v_+ + \dfrac{V}{2} \displaystyle\sum_{k_{1,i} \in \mathcal{M}_1^-(V)} \left(w_+ - w_* + \dfrac{1}{\mathcal{R}(V)\sqrt{L_0(V)}}(w_c - w_*)k_{1,i} \right) \\ \qquad\qquad\qquad \times \dfrac{k_{1,i} P_-(k_{1,i}, V)}{\sin(k_{1,i}/2)} e^{-ik_{1,i}(\xi+1/2)}, \qquad \xi > -\dfrac{1}{2}, \end{cases} \tag{64}$$

where $v_\pm$ once again satisfy the first Rankine-Hugoniot condition (51).

An important difference between the interphase shock and kink solutions is that due to the different behavior of $L_\pm(k, V)$ at infinite k in the case of shocks, the strains $w_\pm$ at infinity are no longer uniquely determined by V, i.e., there is no condition equivalent to (45) we had for kinks. Thus there is *no kinetic relation* $w_\pm = w_\pm(V)$ or $G = G(V)$. Instead, either w_+ or w_- (which are related through (44)) is an additional parameter in the problem, and it is easy to see that the driving force, which in this case reduces to

$$G = \frac{1}{2} \left((c_\gamma^2 - V^2)(w_- - w_c)^2 - (c_1^2 - V^2)(w_c - w_+)^2 \right), \tag{65}$$

is a function of V and either w_+ or w_-, or of w_+ and w_-, by (44). Given any v_+ (which can be set to zero), w_+ and $w_- > w_+$, we can find V and v_- from the Rankine-Hugoniot conditions (44) and (51), respectively, obtain the shock solution given by (62) and (64) and calculate the driving force and hence the rate of energy dissipated by the shock. This reflects on the discrete level the well-known fact that the continuum initial value problem is well-posed in the case of shocks, which unlike kinks satisfy the Lax condition. However, in the case of kinks arbitrarily chosen $w_\pm$ may not be compatible with the kinetic relations (45).
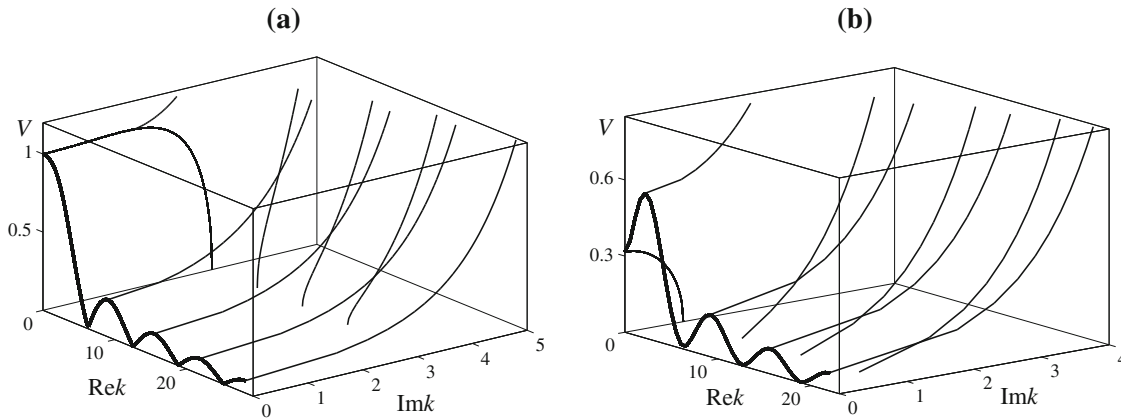
Fig. 5 The structure of roots of $g_\alpha(k, V) = 0$ when **a** $\alpha + 4\beta > 0$ (here $\alpha = 1.2$, $\beta = -0.2$) and **b** $\alpha + 4\beta < 0$ (here $\alpha = 0.6$, $\beta = -0.5$). The *thick curves* correspond to the real roots, and *thin curves* show the non-real root branches. Due to the root symmetry, only the first octant is shown

7 Examples

To illustrate the general solution, we now study in detail the case when only the first and second-neighbor interactions are included, i.e., $q = 2$. In this case, it is convenient to introduce the dimensionless parameter $\beta = 4\Omega_2$ which measures the relative strength of second-neighbor interactions. Then

$$c_1 = \sqrt{1 + \beta}, \quad c_\gamma = \sqrt{\gamma + \beta}.$$

The problem is thus completely determined by two parameters: β and γ. We assume that

$$\beta_c < \beta \le 0, \quad \beta_c = -\min\{1, \gamma\}. \tag{66}$$

The lower bound ensures stability of the uniform deformation in each phase, while the upper bound is motivated by the linearization of the potentials of the Lennard–Jones type [28]. Note that in this case the energy of the chain can be written as

$$\mathcal{E} = \sum_{n=-\infty}^{\infty} \left[\frac{\dot{u}_n^2}{2} + \phi(w_n) - \frac{\beta}{8}(w_n - w_{n-1})^2 \right], \quad \phi(w) = \phi_1(w) + \frac{\beta}{2}w^2,$$

so that $\beta < 0$ introduces a strain-gradient-like interfacial energy term that makes an isolated phase boundary considered here energetically favorable [28]. The case $\beta > 0$ favors multiple interface formation and needs to be treated differently [33].

7.1 Roots of the dispersion relation

We begin by considering the roots of the dispersion relation (20), which in this case reduces to

$$g_\alpha(k, V) = -V^2 k^2 + 4\alpha \sin^2 \frac{k}{2} + \beta \sin^2 k, \quad \alpha = 1, \gamma. \tag{67}$$

The structure of the roots is shown in Fig. 5. As mentioned earlier, the branch of real roots (r, V) can be found explicitly. In this case we obtain (for $V > 0$)

$$V = \frac{1}{|r|}\sqrt{\beta \sin^2 r + 4\alpha \sin^2 \frac{r}{2}};$$

these roots are shown in Fig. 5 by thick curves. We can also find the branch of purely imaginary roots (is, V), where s is real. It is given by

$$V = \frac{1}{|s|}\sqrt{\beta \sinh^2 s + 4\alpha \sinh^2 \frac{s}{2}}.$$

The two branches intersect at the point $(k, V) = (0, c_\alpha)$. The other roots either bifurcate from the local maxima of these branches or emanate from the roots at $V = 0$, given by $k = 2\pi n \pm 2is_\alpha$, where n is any integer and

$$s_\alpha = \operatorname{arccosh}\sqrt{\frac{\alpha}{|\beta|}}. \tag{68}$$

As in [29], we note that there are two types of root structures. Example of the first type of structure is shown in Fig. 5a. It occurs when $\alpha + 4\beta \geq 0$ and thus the point $(k, V) = (0, c_\alpha)$ is the maximum of the real root branch. In this case, the branch (is, V) of purely imaginary roots has a maximum point at nonzero s_m from which complex roots with nonzero real part bifurcate. If $\alpha + 4\beta < 0$, the point $(0, c_\alpha)$ becomes a local minimum, and we obtain the second type of root structure, an example of which is shown in Fig. 5b. In this case, the imaginary root branch has a maximum at $(0, c_\alpha)$, and the real root branch (r, V) has a maximum point at nonzero r_m, from which the complex roots bifurcate. As we shall see, the type of root structure has significant implications in existence and structure of shock and kink solutions, as well as their behavior at velocities near the sonic limit.

7.2 Equilibrium solutions

The equilibrium solutions (57) reduce to

$$w_n = \begin{cases} \dfrac{\sigma + \gamma}{c_\gamma^2} - \left(\dfrac{\sigma + \gamma}{c_\gamma^2} - w_*\right)\dfrac{s_\gamma}{\sinh s_\gamma}P_+(2is_\gamma, 0)\mathrm{e}^{2s_\gamma(n+1/2)}, & n \leq -1, \\[4mm] \dfrac{\sigma}{c_1^2} - \left(\dfrac{\sigma}{c_1^2} - w_*\right)\dfrac{s_1}{\sinh s_1}P_-(-2is_1, 0)\mathrm{e}^{-2s_1(n+1/2)}, & n \geq 0, \end{cases} \tag{69}$$

with s_α defined in (68). It also can be written as

$$w_n = \begin{cases} by^n + \dfrac{\sigma + \gamma}{c_\gamma^2}, & n \leq -1, \\[4mm] ax^n + \dfrac{\sigma}{c_1^2}, & n \geq 0, \end{cases} \tag{70}$$

where

$$a = (c_\gamma - \sqrt{\gamma})\frac{(\gamma - 1)\sigma - c_1^2\gamma}{c_1^2 c_\gamma(1 - \gamma + c_1 + c_\gamma\sqrt{\gamma})}, \quad x = \frac{2}{\beta}(c_1 - 1) - 1;$$

$$b = (c_1 + 1)\frac{(\gamma - 1)\sigma - c_1^2\gamma}{c_1 c_\gamma^2(1 - \gamma + c_1 + c_\gamma\sqrt{\gamma})}, \quad y = -\frac{2}{\beta}(c_\gamma\sqrt{\gamma} + \gamma) - 1;$$

The strain profile is monotonically decreasing, and the stress σ must be within the trapping region (58), where the Peierls stresses (59) reduce to

$$\sigma_P^- = \frac{c_1 c_\gamma}{c_\gamma - \sqrt{\gamma}}\left((1 - c_1 - \sqrt{\gamma} + c_\gamma)w_c + \gamma\frac{c_\gamma - \sqrt{\gamma}}{c_1 + c_\gamma}\cdot\frac{1 + c_1 - \sqrt{\gamma} + c_\gamma}{1 + c_1 - \gamma + c_\gamma\sqrt{\gamma}}\right),$$

$$\sigma_P^+ = \frac{c_1 c_\gamma}{c_\gamma + c_1\sqrt{\gamma}}\left((1 - \sqrt{\gamma})(1 + c_1 + \sqrt{\gamma} - c_\gamma)w_c + \frac{\gamma}{c_1 + c_\gamma}(1 + c_1 - \sqrt{\gamma} + c_\gamma)\right),$$

with the corresponding Peierls values of the driving force given by (60). In particular, $G = G(0+) = G_P^+$ corresponds to the saddle-point equilibrium from which the dynamic solution branch with $V > 0$ bifurcates:

$$w_n = \lim_{V \to 0} w(n - Vt) = \begin{cases} w_c + b(y^n - 1), & n \leq -1, \\ w_c + a(x^n - 1), & n \geq 0. \end{cases} \tag{71}$$

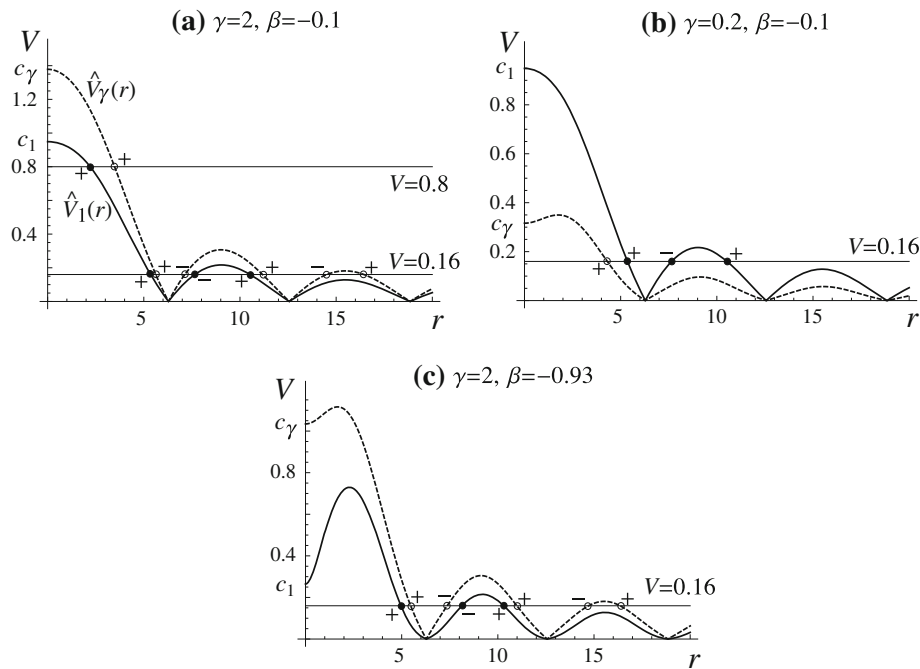**Fig. 6** Positive real roots at different values of γ and β in the kink region. *Black and white circles* mark the roots in $\mathcal{N}_1(V)$ and $\mathcal{N}_\gamma(V)$, respectively, and the *plus and minus signs* indicate whether the corresponding waves appear behind (*plus*) or in front (*minus*) of the phase boundary
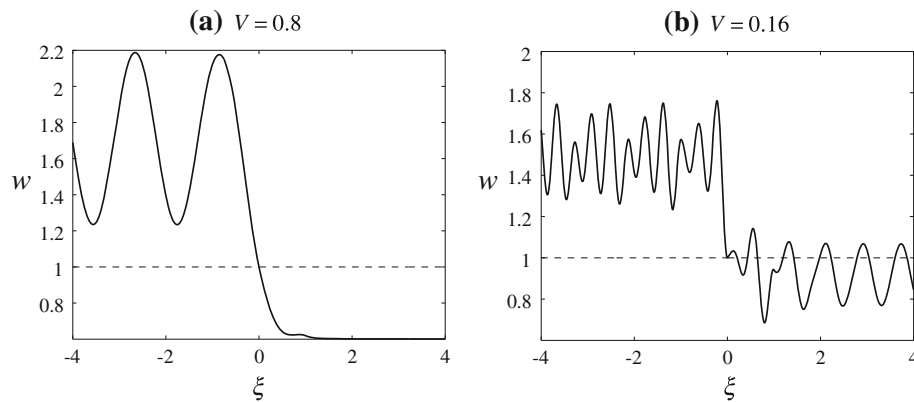

Fig. 7 Kink profiles at **a** $V = 0.8$ and **b** $V = 0.16$. Other parameters are $\gamma = 2$, $\beta = -0.1$, and $w_c = 1$. The solution in (**a**) is admissible, but the solution in (**b**) is not

7.3 Dynamic kinks

We start by considering kink profiles at $\gamma = 2$ and $\beta = -0.1$. In this case, the kink velocities must satisfy $0 \leq V < c_1 \approx 0.95$. The corresponding structure of the real roots is shown in Fig. 6a. When V is below c_1 but above the next resonance velocity, there are two positive real roots, one in $\mathcal{N}_1^+(V)$ and another in $\mathcal{N}_\gamma^+(V)$, which correspond to non-decaying lattice waves propagating behind the phase boundary. An example of such strain profile at $V = 0.8$ is shown in Fig. 7a. One can see that it satisfies the constraints (18) and thus represents an admissible strain profile. Consider now the velocity $V = 0.16$. As shown in Fig. 6a, in this case there are eight real roots, three from $\mathcal{N}_1^\pm$ (black circles) and five from $\mathcal{N}_\gamma^\pm$ (white circles). Five of these roots correspond to the waves appearing behind the phase boundary (two from $\mathcal{N}_1^+$ and three from $\mathcal{N}_\gamma^+$), and the other three (one from $\mathcal{N}_1^-$ and two from $\mathcal{N}_\gamma^-$) yield waves propagating in front. However, the corresponding strain profile,
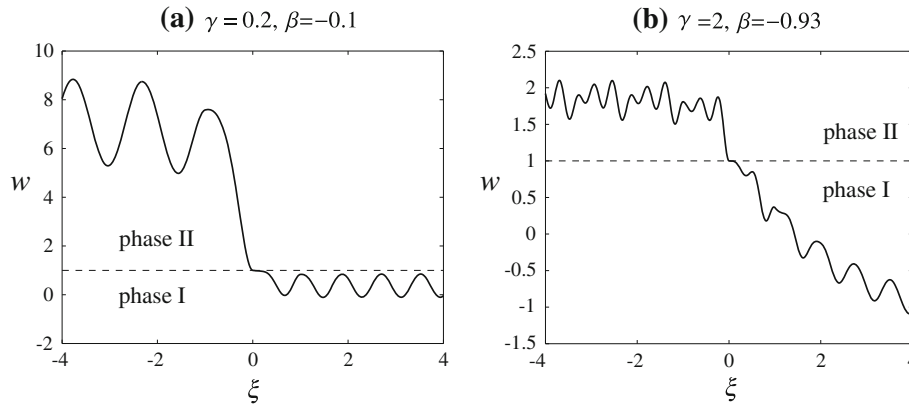
Fig. 8 Kink profiles at $V = 0.16$, $w_c = 1$ and **a** $\gamma = 0.2$, $\beta = -0.1$; **b** $\gamma = 2$, $\beta = -0.93$. Both solutions are admissible

shown in Fig. 7b, violates the constraints (18) and thus has to be discarded. In general, for these parameter values only the kink profiles with velocities $0.33 \leq V < c_1$ are admissible.

Note, however, that for fixed V and β, a sufficiently small value of γ yields an admissible solution. For example, at $\gamma = 0.2$ the traveling wave solution with $V = 0.16$ and $\beta = -0.1$ becomes admissible, as shown in Fig. 8a. The corresponding real roots are shown in Fig. 6b. Clearly, the set $\mathcal{N}_1(0.16)$ remains the same, but the set $\mathcal{N}_\gamma(0.16)$ now contains only one root (placed behind) since the curve $\hat{V}_\gamma(r)$ is now substantially below $\hat{V}_1(r)$. Note also that the larger $|\beta|/\gamma$ in this case implies smaller s_γ in (68) and thus the purely imaginary roots of $g_\gamma(k, V)$ are closer to the origin. The resulting wider boundary layer structure around the phase boundary prevents the oscillations ahead of the front from crossing over into the phase II region. Similarly, a sufficiently large $|\beta|$ also yields an admissible solution at fixed V and γ: see Fig. 8b for an admissible profile at $V = 0.16$, $\gamma = 2$ and $\beta = -0.93$. Observe that the real root structure at $V = 0.16$ is not significantly affected by the larger $|\beta|$ (compare parts (a) and (c) in Fig. 6a). However, the boundary layer effect described above is more pronounced in this case because increasing $|\beta|$ reduces both s_γ and s_1 in (68), making purely imaginary roots of both $g_\gamma(k, V)$ and $g_1(k, V)$ closer to the origin.

7.4 Kinetic relations

Kinetic relations (53) at fixed $\beta = -0.1$ and different values of γ are shown in Fig. 9 (solid curves) along with the corresponding values $G(0+) = G_P^+$ of the upper Peierls driving force. As discussed above, not all traveling wave solutions are admissible, and the corresponding low-velocity portions of the kinetic curves need to be removed. One can see that both the upper bound G_P^+ of the trapping region and the minimal driving force for dynamic kinks decrease as γ increases.

Note also that at $\gamma \neq 1$ the driving force is continuous at the resonance velocities. Indeed, as V approaches a resonance velocity (local maximum) from below we have two positive real roots, $r_\alpha^+(V) \in \mathcal{N}_\alpha^+(V)$ and $r_\alpha^-(V) \in \mathcal{N}_\alpha^-(V)$ approach the same value at the maximum point, so that their ratio $r_\alpha^+(V)/r_\alpha^-(V)$, which enters in $\mathcal{R}(V)$ via (40), tends to 1. Here, we have either $\alpha = \gamma$ or $\alpha = 1$. For velocities above the resonance value these roots disappear, and thus $\mathcal{R}(V)$ approaches the same value from above. By (53), the continuity of $\mathcal{R}(V)$ implies that $G(V)$ is also continuous when $\gamma \neq 1$ (note, however, that its derivative has a finite jump discontinuity at each resonance speed). It is not hard to see that this is also true in the general case $q \geq 2$, where resonance velocities may correspond to either maximum or minimum points. As $\gamma \to 1$, the derivative of the driving force becomes larger as velocity approaches a resonance value from below (see (b) and (c) in Fig. 9), and in the limiting case $\gamma = 1$ of equal slopes there is an infinite resonance at these values [29].

The behavior of the driving force as V approaches the sonic limit $c_{\min} = \min\{c_1, c_\gamma\}$ from below depends on the structure of the real roots, which is in turn determined by β and γ. To see this, note that at $0 < V < c_{\min}$ the sets $\mathcal{N}_1^+(V)$ and $\mathcal{N}_\gamma^+(V)$ each have only one root in the interval $(0, 2\pi)$, and there are no other positive real roots in this interval. Denote these roots by $r_{1,1}(V) \in \mathcal{N}_1^+(V)$ and $r_{\gamma,1}(V) \in \mathcal{N}_\gamma^+(V)$ and observe that $\mathcal{R}(V)$ in (40) includes the factor $r_{\gamma,1}(V)/r_{1,1}(V)$. If $\gamma > 1$, the kinetic relation tends to a finite value from below for any β. Indeed, in this case $c_{\min} = c_1$ and thus if $1 + 4\beta > 0$, we have $r_{1,1}(V) \to 0$ as $V \to c_1 - 0$
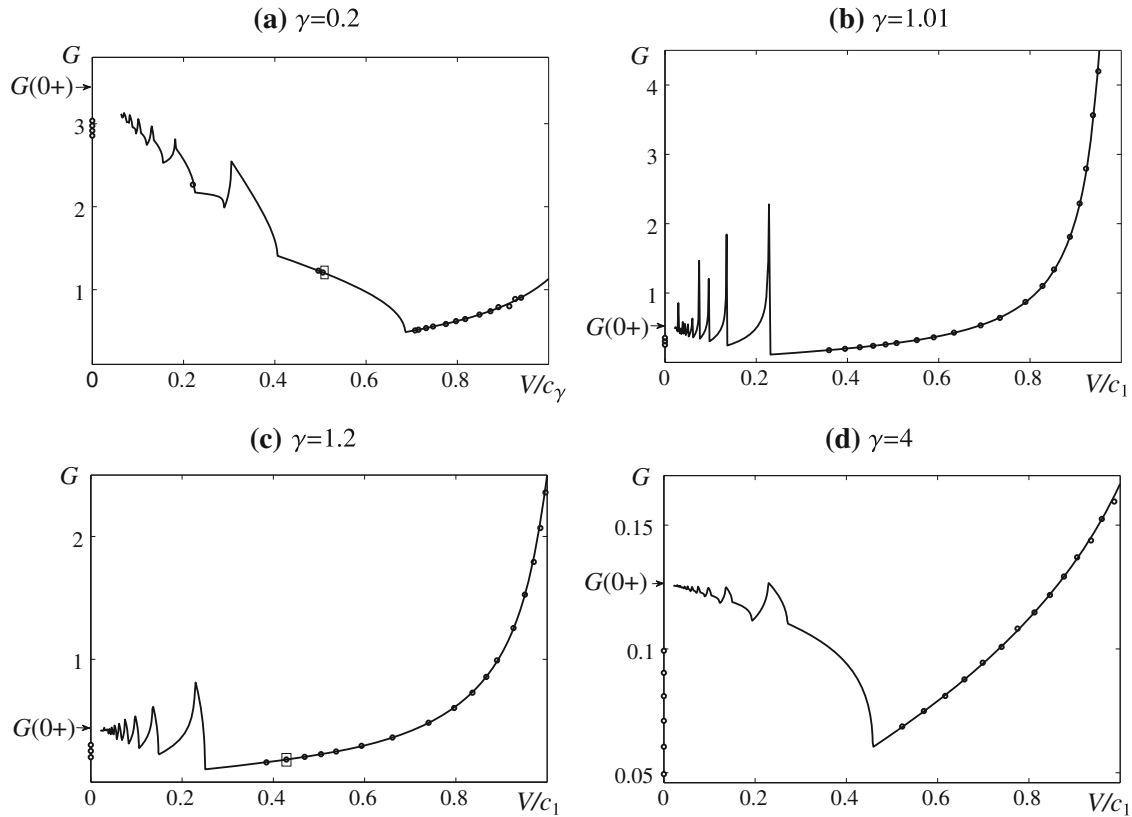
Fig. 9 Kinetic relations (*solid curves*) for kinks at $\beta = -0.1$ and different values of γ and the results of numerical simulations of the Riemann problem (*circles*). Solutions corresponding to the points inside *rectangles* are shown in Figs. 13 and 14

since $(0, c_1)$ is the maximum point (e.g., Fig. 6a), while $r_{\gamma,1}(V)$ has a nonzero limit. Other positive real roots $r > 2\pi$ either disappear or tend to nonzero values in the limit. This means that $\mathcal{R}(V) \to \infty$, and hence the driving force tends to a finite value as V approaches the sonic limit from below:

$$G(V) \to G_s = \frac{\gamma - 1}{2} (w_c - w_*)^2 \,;$$

in parts (b), (c) and (d) of Fig. 9 the values of G_s are 50, 2.5, and 1/6, respectively. Note that in view of (13) G_s becomes infinite when $\gamma = 1$ (equal slopes). If $1 + 4\beta < 0$, $(0, c_1)$ is a local minimum, and all positive real roots tend to nonzero values as $V \to c_1 - 0$, implying a finite limit of $\mathcal{R}(V)$ and hence $G(V)$.

If $\gamma < 1$, we have $c_{\min} = c_\gamma$. In this case, the limit is finite if $\gamma + 4\beta < 0$, for the same reason as above (the limits of all positive real roots are nonzero); see Fig. 9a. When $\gamma + 4\beta > 0$, $\mathcal{R}(V) \to 0$ and hence $G(V) \to \infty$ in the sonic limit because in this case $r_{\gamma,1}(V)$ approaches zero, while $r_{1,1}(V)$ tends to a nonzero value.

7.5 Interphase shocks

Consider now the interphase shocks solutions. Recall that they can only occur at $\gamma > 1$ and that the shock velocities satisfy $c_1 < V < c_\gamma$. In what follows, we will fix the average strain w_+ in front of the shock, which is a free parameter in this case, at zero. As in the case of kinks, the two different types of root structure affect the admissibility and the form of shock solutions. For fixed $\gamma = 2$ the two cases are illustrated in Fig. 10. In the first case we have $1 + 4\beta > 0$, so that the point $(0, c_1)$ is the maximum. This implies that all shock solutions have only one radiative mode, corresponding to a single root in $\mathcal{N}_\gamma^+(V)$ and thus propagating behind the shock. For $\gamma = 2$, $\beta = -0.1$, and $V = 1.05$ this root is shown in Fig. 10a, and the corresponding admissible strain profile is shown in Fig. 11a. Our calculations suggest that for this type of root structure all interphase shock solutions are admissible.
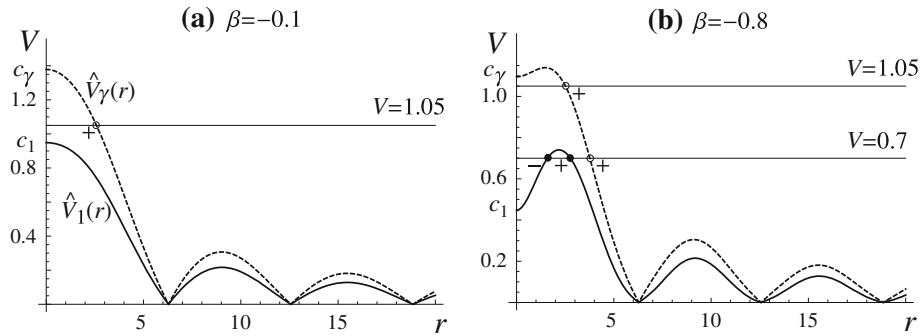
Fig. 10 Positive real roots at $\gamma = 2$ and different values of β in the shock region. *Black and white circles* mark the roots in $\mathcal{N}_1(V)$ and $\mathcal{N}_\gamma(V)$, respectively, and the *plus and minus signs* indicate whether the corresponding waves appear behind (*plus*) or in front (*minus*) of the phase boundary
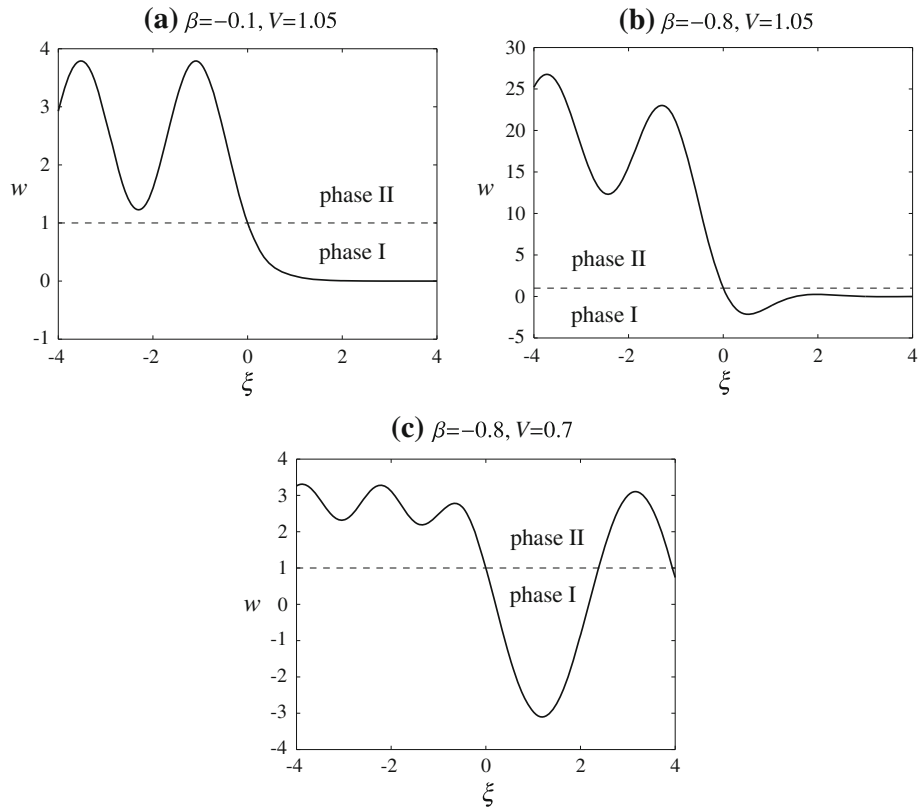

Fig. 11 Shock profiles at $\gamma = 2$, $w_c = 1$, $w_+ = 0$ and **a** $V = 1.05$, $\beta = -0.1$; **b** $V = 1.05$, $\beta = -0.8$; **c** $V = 0.7$, $\beta = -0.8$. Solutions in (**a**) and (**b**) are admissible, while solution in (**c**) is not

Consider now $\beta = -0.8$, when $1 + 4\beta < 0$ and $(0, c_1)$ is a local minimum. At $V = 1.05$, which is above the maximum of $\hat{V}_1(r)$, we still have a single mode propagating behind (see Fig. 10b), and the corresponding admissible strain profile is shown in Fig. 11b. If, however, the shock velocity is below the maximum of $\hat{V}_1(r)$, two additional radiative modes appear due to roots of $g_1(r, V)$, one propagating behind and the other in front. This is illustrated in Fig. 10b for $V = 0.7$. The corresponding solution, shown in Fig. 11c, is not admissible because the large-amplitude mode in front violates the constraints (18). In fact, our calculations suggest that only interphase shocks with velocities above the maximum of $\hat{V}_1(r)$ that have a single radiative mode
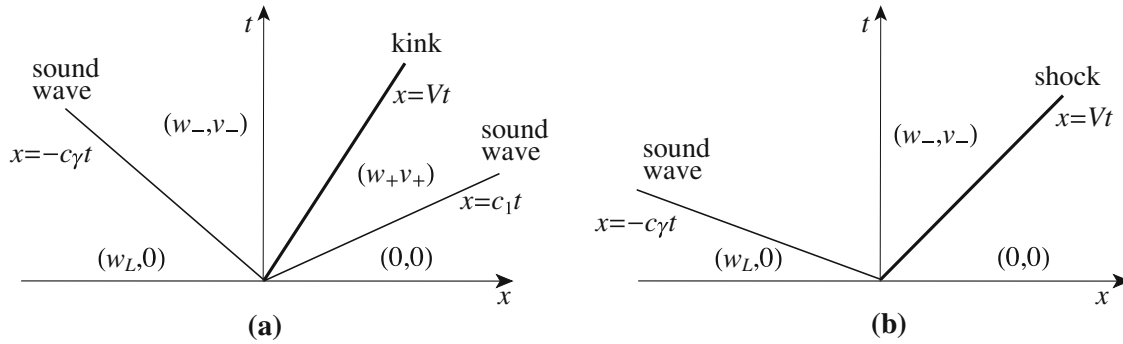
Fig. 12 Self-similar macroscopic solution of the Riemann problem with a single phase boundary that is (**a**) a kink and (**b**) a shock

propagating behind the interface are admissible in the case $1 + 4\beta < 0$.[3] Note also that when $\gamma + 4\beta < 0$, as is the case in Fig. 10b, the wave number of the radiative mode propagating behind approaches a finite value when $V \to c_\gamma - 0$, whereas at $\gamma + 4\beta > 0$ it tends to zero.

8 Stability of the traveling wave solutions

To study stability of the admissible traveling wave solutions, we numerically solve the equations (10) subject to the Riemann initial data that consists of piecewise constant strain

$$w_n(0) = \begin{cases} w_L, & n < n_0, \\ w_c, & n = n_0, \\ 0, & n > n_0. \end{cases} \tag{72}$$

and zero initial particle velocity. We assume that $w_L > w_c > 0$, so that the initial strain profile has a phase boundary at $n = n_0$.

On the macroscopic level, we expect to see a self-similar solution shown in Fig. 12. As before, subsonic and intersonic phase boundaries need to be considered separately.

8.1 Stability of kinks

If the phase boundary is a kink, there are two sound waves (single-phase shock waves), one behind the kink and propagating with speed $c_\gamma > V$ in the opposite direction, and another one moving ahead of the kink with velocity $c_1 > V$; see Fig. 12a. Rankine–Hugoniot jump conditions across each sound wave and across the phase boundary then result in the following relationships between the left initial strain w_L, the velocity V, and the strain $w_\pm$ in front and behind the phase boundary:

$$w_- = \frac{c_\gamma(c_1 + V)w_L + \gamma}{(c_1 + c_\gamma)(c_\gamma + V)}, \qquad w_+ = \frac{c_\gamma(c_\gamma - V)w_L - \gamma}{(c_1 + c_\gamma)(c_1 - V)}. \tag{73}$$

As remarked in Sect. 1, one can see that in the absence of a kinetic relation that yields $w_\pm$ as functions of V, the macroscopic Riemann problem would have an infinite number of solutions parameterized by the velocity V of the kink. Having solved the discrete problem, however, we now have the relations $w_\pm = w_\pm(V)$, given by (45) (or, equivalently, by the kinetic relation (53)), which select a unique velocity V for a given left initial strain w_L, provided that the corresponding traveling wave solution exists and is stable.

To investigate stability of the obtained subsonic traveling wave solutions, we conducted numerical simulations of the Riemann problem for the discrete system (10) on a truncated chain with 600 lattice points for an increasing sequence of values of the initial strain w_L in (72). For w_L below a certain threshold value, the long-time solution featured a trapped phase boundary ($V = 0$) with sound waves propagating away from it.

---

[3] In general, admissibility of shock solutions also depends on the choice of w_+. Larger w_+ makes the interval of admissibility narrower.
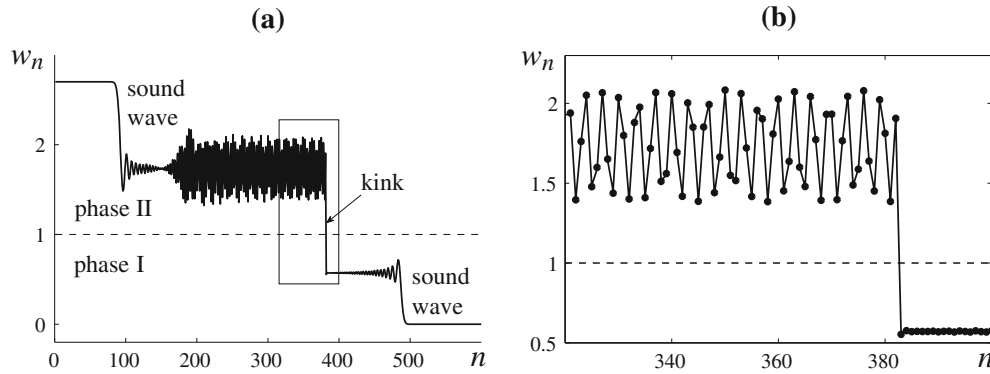
Fig. 13 a Solution of the Riemann problem $w_n(t)$ at $t = 200$, $w_L = 2.7$, $V = 0.4065$, $\gamma = 1.2$, $\beta = -0.1$, and $w_c = 1$. **b** Numerical solution (*circles*) inside the rectangle in (**a**) and the traveling wave solution (*solid line*)
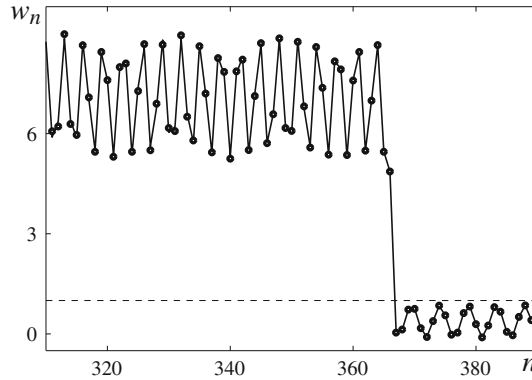

Fig. 14 Solution of the Riemann problem $w_n(t)$ around the phase boundary (*circles*) and the corresponding traveling wave solution (*solid line*) at $t = 400$, $w_L = 11.6$, $V = 0.16$, $\gamma = 0.2$, $\beta = -0.1$, and $w_c = 1$

At some parameter values, e.g., $\gamma = -0.2$, $\beta = -0.1$, and $w_c = 1$, formation and annihilation of additional phase boundaries was also seen in this regime, due to the oscillations behind the sound wave propagating ahead. At higher w_L a steady motion of the phase boundary with some nonzero velocity V was typically observed after an initial transient period. Using (73) for given w_L and V, we then computed the driving force (52) and compared it to the value given by the kinetic relation $G = G(V)$. If the numerical solution around the phase boundary approaches the corresponding traveling wave solution, implying its stability, the difference between these two values should be small. The results of the simulations at $\beta = -0.1$, $w_c = 1$ and different values of γ are shown in Fig. 9. They suggest that kinks that travel sufficiently fast are stable, in agreement with the observation made in [29] for the case $\gamma = 1$. These solutions typically have velocities between the sound speed $c_{\min} = \min\{c_1, c_\gamma\}$ and the next resonance velocity and feature lattice waves that propagate only behind the phase boundary. An example of such solution is shown in Fig. 13.

One can see that the structure of the long-time solution is as predicted by the macroscopic theory (Fig. 12a), with two sound waves propagating away from the kink, but in the discrete problem the piecewise constant macroscopic strain is superimposed with oscillations due to lattice dispersion. Note that the numerical solution zoomed around the phase boundary (circles in Fig. 13b) is in perfect agreement with the analytical traveling wave solution (solid line).

Recall that when γ is sufficiently small (or when $|\beta|$ is large enough), traveling wave solutions with smaller velocities may become admissible. Figure 9a suggests that some of these admissible kinks may be also stable. An example of such solution at $\gamma = 0.2$, $\beta = -0.1$ and $V = 0.16$ is shown in Fig. 14. Note that in this case the moving kink emits lattice waves in both directions.

Based on [32], where a trilinear up–down–up stress–strain law with equal moduli was considered, we expect that introducing a sufficiently wide spinodal region will result in more admissible and stable solutions in the low-velocity regime since the nonlinearity tends to reduce the amplitude of lattice waves. For the case of different elastic moduli this problem will be analyzed elsewhere.
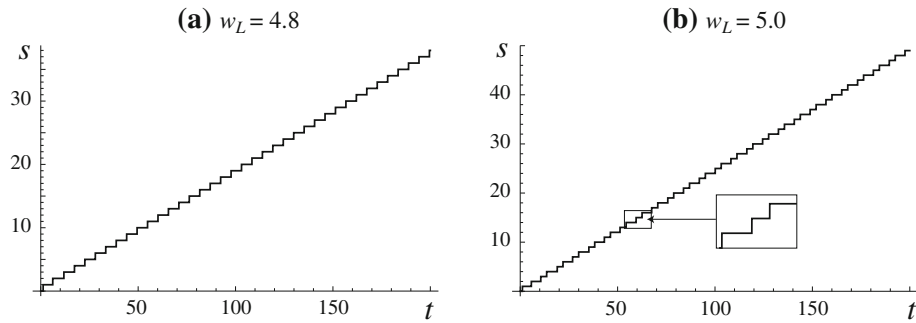
Fig. 15 The position $s(t)$ of the phase boundary in the solution of the Riemann problem at $\gamma = 1.2$, $\beta = -0.8$, $w_c = 2$, and **a** $w_L = 4.8$; **b** $w_L = 5.0$. In (**a**) the solution approaches the steady kink motion with $V = 0.1866$, while in (**b**) the limiting solution is characterized by front velocity that oscillates between two different values

We found that when $|\beta|$ is very large, there are also other attractors that do not have a traveling wave form near the phase boundary and feature a non-steady kink motion with velocity oscillating about some average value. Such solutions are usually seen for a small interval of w_L values above and below which the attractors are again the traveling waves. Consider, for example, the position $s(t)$ of the front at $\gamma = 1.2$, $\beta = -0.8$, and $w_c = 2$. At $w_L = 4.8$ the numerical solution quickly approaches a steady motion, as shown in Fig. 15a, with velocity $V = 0.1866$. This motion is described by the corresponding traveling wave solution. Like the solution shown in Fig. 14, this solution is a slower kink with lattice waves propagating in both directions. The same is true for $4.5 \le w_L \le 4.9$, and for $w_L \ge 6$ the numerical solution around the phase boundary approaches a fast traveling wave that oscillations behind the front. However, for the intermediate values of the left initial strain the attractor is different. For instance, at $w_L = 5$ the motion of the front is no longer described by the traveling wave ansatz, as can be seen in Fig. 15b. Instead, the time intervals over which the phase boundary advances by one lattice space continue to oscillate between the values 3.08 and 5.05 even at large times.

We plan to explore such breather-like attractors in the future work.

8.2 Stability of interphase shocks

If $\gamma > 1$ and the initial left strain w_L is sufficiently high, the phase boundary becomes a shock with $w_+ = 0$ and $c_1 < V < c_\gamma$. The structure of the corresponding macroscopic solution is shown in Fig. 12b. Applying the Rankine-Hugoniot conditions across the interphase shock and the sound wave propagating behind, one obtains the average strain behind the phase boundary and the relationship between V and w_L:

$$w_- = \frac{\gamma}{c_\gamma^2 - V^2}, \quad w_L = \frac{\gamma(c_\gamma + V)}{c_\gamma(c_\gamma^2 - V^2)}. \tag{74}$$

Inverting the second equation in (74), one can obtain a unique shock velocity for given w_L, find the corresponding w_- and compute the driving force (65), which reduces to

$$G = \frac{\gamma^2}{2(c_\gamma^2 - V^2)} + \frac{(\gamma - 1)w_c^2}{2} - \gamma w_c.$$

since $w_+ = 0$. This function is plotted in Fig. 16 at $\gamma = 2$ and two different values of β (solid lines), along with the results of the numerical simulations (circles).

At $\beta = -0.1$, the numerical solutions of the Riemann problem for the discrete system exhibit a single interface with V and w_- very close to the ones predicted by (74) for the entire range of w_L that corresponds to $c_1 < V < c_\gamma$; see Fig. 16a. Around the phase boundary numerical solutions converge to the corresponding traveling wave solutions, which in this case are admissible in the entire shock interval. See, for example, the comparison of numerical and analytical solutions at $V = 1.05$ in Fig. 17a.

Meanwhile, at $\beta = -0.8$ the numerical simulations with the initial data that corresponds to velocities below the resonance velocity $V_{res} \approx 0.7406$ (the maximum of $\hat{V}_1(r)$ in Fig. 10a) result in formation of multiple phase boundaries; see Fig. 18 for an example.

(a) $\beta = -0.1$ **(b)** $\beta = -0.8$
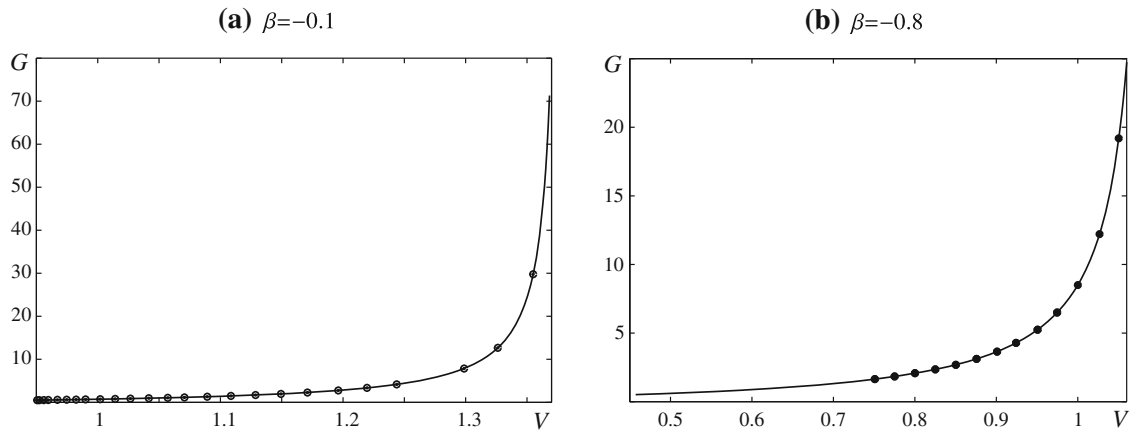

Fig. 16 Driving force as the function of velocity for interphase shock solutions of the Riemann problem as predicted by continuum theory (*solid line*) and numerical simulations of the discrete model (*circles*) at $\gamma = 2$ and **a** $\beta = -0.1$; **b** $\beta = -0.8$
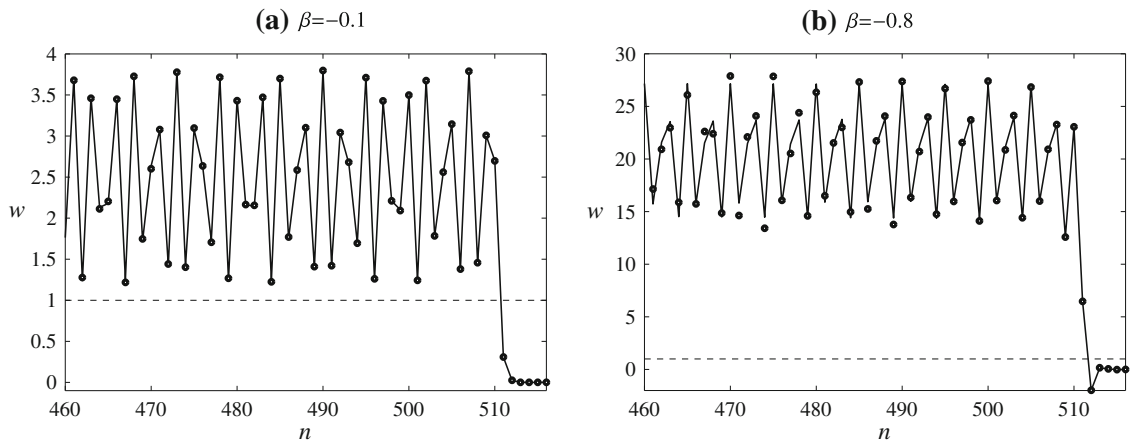
(a) $\beta = -0.1$ **(b)** $\beta = -0.8$

Fig. 17 Solutions of the Riemann problem $w_n(t)$ around the phase boundary (*circles*) and the corresponding traveling wave solutions (*solid lines*) at $t = 200$, $V = 1.05$, $\gamma = 2$, $w_c = 1$ and **a** $\beta = -0.1$; **b** $\beta = -0.8$. The corresponding traveling wave profiles $w(\xi)$ are shown in Fig. 11a, b
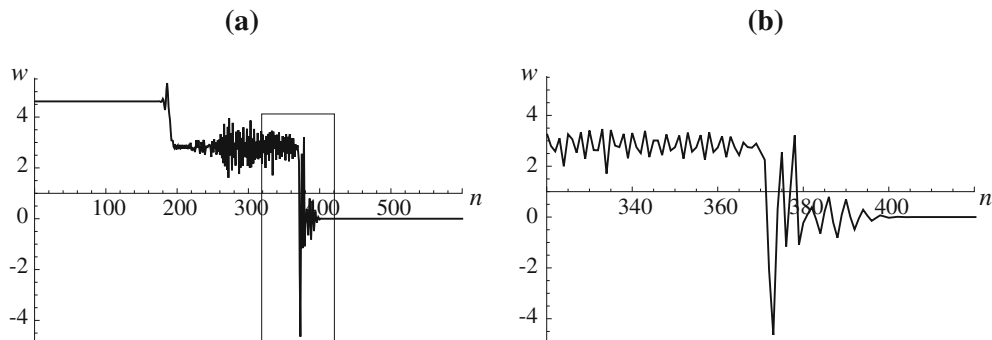
(a)   **(b)**

Fig. 18 a Solution of the Riemann problem $w_n(t)$ with multiple phase boundaries. **b** Zoom-in of the rectangle in part (**a**). Here, $t = 100$, $w_c = 1$, $\gamma = 2$, $\beta = -0.8$, and $w_L = 4.6169$, which corresponds to $V = 0.7$ according to (74). The corresponding traveling wave solution is not admissible, as shown in Fig. 11c

Recall that the corresponding traveling wave solutions are not admissible, e.g., see Fig. 11c. When the initial data yield $V_{res} < V < c_\gamma$, only one phase boundary forms. These simulations are shown by circles in Fig. 16b. In each simulation with such initial data the numerical solution around the phase boundary converges to the corresponding admissible traveling wave solution; see, for example, Fig. 17b.

Appendix: Proof of the Proposition

Let V be a non-resonance velocity. We first show that

$$|\mathcal{N}_\alpha^+(V)| = \begin{cases} |\mathcal{N}_\alpha^-(V)| + 1, & 0 < V < c_\alpha \\ |\mathcal{N}_\alpha^-(V)|, & V > c_\alpha \end{cases}. \tag{75}$$

Fix V such that $0 < V < c_\alpha$. The real roots can be found from the equation $\hat{V}_\alpha(r) = V$, where we recall (26). On every interval $[2\pi n, 2\pi(n+1)]$, where n is a positive integer, the curve $\hat{V}_\alpha(r)$ can intersect the horizontal line corresponding to V an even number of times because it is a continuous nonnegative function that vanishes at the ends of the interval and must have nonzero derivative at the intersections (if there are any) since V is a non-resonance velocity. The points of intersections belong to $\mathcal{N}_\alpha(V)$. The points where $\hat{V}_\alpha(r)$ increases belong to the set $\mathcal{N}_\alpha^-(V)$, and the points where it decreases belong to $\mathcal{N}_\alpha^+(V)$. For each point from $\mathcal{N}_\alpha^-(V)$ there is a corresponding point from $\mathcal{N}_\alpha^+(V)$ and hence on every such interval the number of roots in both sets is same. Now consider the interval $[0, 2\pi]$. Recall that $V(0) = c_\alpha > 0$ and $V < c_\alpha$. The smallest positive root $r_{\alpha,1} \in [0, 2\pi]$ is a point of intersection where the function decreases, and hence it belongs to the set $\mathcal{N}_\alpha^+(V)$; it does not have a corresponding root in the set $\mathcal{N}_\alpha^-(V)$. If there are other roots in the interval $(r_{\alpha,1}, 2\pi]$, they appear in pairs by the same argument. Thus, the first case in (75) holds.

To show the second case, observe that when V approaches the sound speed c_α from below, the first root $r_{\alpha,1}$ in $\mathcal{N}_\alpha^+(V)$ disappears if $r = 0$ is a point of a local maximum of $\hat{V}_\alpha(r)$, and the number of roots in $\mathcal{N}_\alpha^+(V)$ decreases by one. If $r = 0$ is a local minimum, then a new smaller root appears on the increasing part of the curve $\hat{V}_\alpha(r)$. This root belongs to the set $\mathcal{N}_1^-(V)$ and increases the number of elements in this set by one. In either case, the number of elements in the two sets becomes the same for $V > c_\alpha$.

Thus, for a kink velocity, which satisfies $0 < V < \min\{c_1, c_\gamma\}$, the first case in (75) holds for both $\alpha = 1$ and $\alpha = \gamma$. Meanwhile, for a shock velocity, $c_1 < V < c_\gamma$, the first case in (75) holds only for $\alpha = \gamma$, and the second case is true for $\alpha = 1$, proving the Proposition. □

References

1. Abeyaratne, R., Knowles, J.K.: Kinetic relations and the propagation of phase boundaries in solids. Arch. Ration. Mech. Anal. **114**, 119–154 (1991)
2. Atkinson, W., Cabrera, N.: Motion of a Frenkel-Kontorova dislocation in a one-dimensional crystal. Phys. Rev. A **138**(3), 763–766 (1965)
3. Bhattacharya, K.: Microstructure of Martensite—Why It Forms and How It Gives Rise to the Shape-Memory Effect. Oxford University Press, USA (2003)
4. Celli, V., Flytzanis, N.: Motion of a screw dislocation in a crystal. J. Appl. Phys. **41**(11), 4443–4447 (1970)
5. Dafermos, C.M.: Hyperbolic Conservation Laws in Continuum Physics. Springer, Heidelberg (2000)
6. Ericksen, J.L.: Equilibrium of bars. J. Elast. **5**, 191–202 (1975)
7. Escobar, J.C., Clifton, R.J.: On pressure-shear plate impact for studying the kinetics of stress-induced phase transformations. J. Mater. Sci. Eng. A **170**, 125–142 (1993)
8. Escobar, J.C., Clifton, R.J.: Pressure-shear impact-induced phase transitions in Cu-14.4Al-4.19Ni single crystals. SPIE **2427**, 186–197 (1995)
9. Ishioka, S.: Uniform motion of a screw dislocation in a lattice. J. Phys. Soc. Jpn. **30**, 323–327 (1971)
10. Kresse, O., Truskinovsky, L.: Mobility of lattice defects: discrete and continuum approaches. J. Mech. Phys. Solids **51**, 1305–1332 (2003)
11. Kresse, O., Truskinovsky, L.: Lattice friction for crystalline defects: from dislocations to cracks. J. Mech. Phys. Solids **52**, 2521–2543 (2004)
12. LeFloch, P.G.: Hyperbolic Systems of Conservation Laws. ETH Lecture Note Series. Birkhäuser, Basel (2002)
13. Marder, M., Gross, S.: Origin of crack tip instabilities. J. Mech. Phys. Solids **43**(1), 1–48 (1995)

14. Noble, B.: Methods Based on the Wiener–Hopf Technique for the Solution of Partial Differential Equations. 2nd edn. Chelsea Publishing Company, New York (1988)
15. Niemczura, J., Ravi-Chandar, K.: Dynamics of propagating phase boundaries in NiTi. J. Mech. Phys. Solids **54**, 2136–2161 (2006)
16. Serre, D.: Systems of Conservation Laws, Volume 1, 2. Cambridge University Press, Cambridge (1999)
17. Shaw, J.A., Kyriakides, S.: On the nucleation and propagation of phase transformation fronts in a NiTi alloy. Acta Mater. **45**, 683–700 (1997)
18. Slemrod, M.: Admissibility criteria for propagating phase boundaries in a van der Waals fluid. Arch. Ration. Mech. Anal. **81**, 301–315 (1983)
19. Slepyan, L.I.: Antiplane problem of a crack in a lattice. Mech. Solids **16**(5), 101–115 (1982)
20. Slepyan, L.I.: Models and Phenomena in Fracture Mechanics. Springer, Berlin (2002)
21. Slepyan, L.I., Troyankina, L.V.: Fracture wave in a chain structure. J. Appl. Mech. Tech. Phys. **25**(6), 921–927 (1984)
22. Slepyan, L.I., Troyankina L.V.: Impact waves in a nonlinear chain. In: Gol'dstein, R.V. (ed.) Plasticity and Fracture of Solids, pp. 175–186. Nauka, Moscow (in Russian) (1988)
23. Slepyan, L.I., Cherkaev, A., Cherkaev, E.: Transition waves in bistable structures. II. Analytical solution: wave speed and energy dissipation. J. Mech. Phys. Solids **53**, 407–436 (2005)
24. Titchmarsh, E.C.: Theory of Functions. 2nd edn. Oxford University press, USA (1976)
25. Truskinovsky, L.: Equilibrium interphase boundaries. Sov. Phys. Doklady **27**, 306–331 (1982)
26. Truskinovsky, L.: Dynamics of nonequilibrium phase boundaries in a heat conducting elastic medium. J. Appl. Math. Mech. **51**, 777–784 (1987)
27. Truskinovsky, L.: Kinks versus Shocks. In Fosdick, R., Dunn, E., Slemrod, M. (eds.) Shock Induced Transitions and Phase Structures in General Media, The IMA Volumes in Mathematics and Its Applications, vol. 52, pp. 185–229. Springer, Berlin (1993)
28. Truskinovsky, L., Vainchtein, A.: The origin of nucleation peak in transformational plasticity. J. Mech. Phys. Solids **52**, 1421–1446 (2004)
29. Truskinovsky, L., Vainchtein, A.: Kinetics of martensitic phase transitions: Lattice model. SIAM J. Appl. Math. **66**, 533–553 (2005)
30. Truskinovsky, L., Vainchtein, A.: Quasicontinuum modelling of short-wave instabilities in crystal lattices. Phil. Mag. **85**(33–35), 4055–4065 (2005)
31. Truskinovsky, L., Vainchtein, A.: Dynamics of martensitic phase boundaries: discreteness, dissipation and inertia. Cont. Mech. Thermodyn. **20**(2), 97–122 (2008)
32. Vainchtein, A.: The role of spinodal region in the kinetics of lattice phase transitions. J. Mech. Phys. Solids **58**(2), 227–240 (2010)
33. Vainchtein, A., Van Vleck, E.S.: Nucleation and propagation of phase mixtures in a bistable chain. Phys. Rev. B **79**(14), 144123 (2009)